Intern rapport; IR 2003-07

KNMI

Synthetic water vapour images from the HIRLAM model using a radiative transfer model

M.H. Voogt

Koninklijk Nederlands Meteorologisch Instituut

De Bilt, 2003

Intern rapport; IR 2003-07

De Bilt, 2003

PO Box 201
3730 AE De Bilt
Wilhelminalaan 10
http://www.knmi.nl
Telephone +31 30 22 06 911
Telefax +31 30 22 10 407

Auteur: Voogt, M.H.

De reeks Intern rapport is in juli 2000 gestart en geeft bij afsluiting de vorderingen rond een project of instrument weer.
De inhoud is primair bestemd voor KNMI-ers, maar de publicaties zijn verder openbaar.
Lezers van buiten het instituut dienen er echter wel rekening mee te houden dat het gebruikte jargon niet in alle gevallen voor buitenstaanders duidelijk zal zijn.

Contents

Preface

This report contains the results of my master's thesis research at the Climate Variability Research section of the Royal Netherlands Meteorological Institute (KNMI), as part of my study Soil, Water, Atmosphere at Wageningen University (WU). I would like to thank my first supervisor Dr. Wim Verkleij (KNMI), for his advice, interest and enthusiasm during the project.

Furthermore I would like to thank Dr. Sander Tijm from the section Research and Development Numerical Modelling, for giving me the HIRLAM data for some gridpoints and his willingness to perform reference calculations with his own method, which is used in the operational weather department at KNMI. I am pleased that my research has suggested some improvements of his method.

I am grateful to Dr. Rob van Dorland, Dr. Wouter Knap and Mr. Rob Roebeling from the Atmospheric Research section, who have helped me in a few theoretical and practical matters concerning radiative transfer.

Finally, I would like to express a word of thanks to my second supervisor Dr. Leo Kroon (WU), who gave useful advice.

M.H.Voogt, December 2003

Summary

In this study, a simple radiative transfer model is developed for the calculation of radiance profiles in the water vapour absorption band (5.7-7.1μm). The model is based on the formal solution of the Schwarzschild equation for radiative transfer. Pressure, temperature and specific humidity fields from the HIRLAM model are used as input. Apart from calculating radiance profiles, the model is also used to construct water vapour images (synthetic water vapour images). For that purpose, the value of the brightness temperature (directly linked to the radiance) at the top of the atmosphere is calculated for a field of gridpoints.

Water vapour images are often interpreted in terms of the tropopause temperature. This is based on the assumption that the troposphere contains enough water vapour in order to fully absorb the upwelling radiation and that the stratosphere is completely dry. As a result, a water vapour image would reflect the altitude of the tropopause. This is a special application of the topographic concept, which states that a water vapour image reflects the altitude of the top of a moist layer.

The model enables us to investigate which part of the atmosphere contributes to the radiation that reaches the top of the atmosphere. We show that the vertical distribution of water vapour throughout the atmosphere is the most important factor. The assumption of full absorption in the troposphere is shown not to hold. Although it is not the height of the tropopause that is reflected in a water vapour image, the topographic concept may still be applied in order to detect sharp boundaries in large structures. Images of the tropopause temperature may show structures that synthetic water vapour images, as constructed by the radiative transfer model, do not show. Although synthetic water vapour images resemble real water vapour images, not all structures are represented well.

Brightness temperature profiles can also be calculated using a method developed by Tijm (KNMI). Tijm did not base his method on radiative transfer, but intuitively described the effect of absorption by water vapour on the brightness temperature profile. After including the pressure and temperature dependence of the absorption, Tijm's method gives results that are almost identical to the results of our model. It is demonstrated that this is not a coincidence by showing that Tijm's method actually integrates a simplified version of the equations for radiative transfer. For the construction of water vapour images, Tijm's method is superior to ours, because Tijm's method requires considerable less computation time. However, the disadvantage of Tijm's method is that it does not give insight in the radiance contribution throughout the atmosphere, as does our method.

Chapter 1

Introduction

In research on cyclone development, potential vorticity has become a valuable parameter (e.g. [18]). The main properties of potential vorticity that are valuable in understanding dynamic processes are its material conservation and invertibility. Material conservation makes it possible to detect whether the origin of air parcels is tropospheric or stratospheric, because the potential vorticity in the stratosphere is higher than in the troposphere, due to higher static stability above the tropopause. The invertibility principle that holds in hydrostatic and geostrophic equilibrium, implies that if the potential vorticity field is known, all other fields such as wind, pressure and temperature, can be derived [6].

Water vapour images give an indication of the humidity in the upper troposphere, because water vapour in the atmosphere very effectively absorbs upwelling radiation in the wavelength band 5.7-7.1μm. In general, the upper troposphere, between 200 and 600 hPa, contributes most to the radiation measured by a satellite [13]. Because the temperature in the troposphere decreases with height, a water vapour image gives information about the height from which radiation is emitted. The topographic concept states that a water vapour image reflects the altitude of the top of a moist layer.

Structures in water vapour images are closely related to the upper level potential vorticity distribution. This is the result of the fact that the troposphere and stratosphere differ in both humidity and potential vorticity. Simplified, the link is that the humid troposphere has low potential vorticity values, whereas the potential vorticity has high values in the dry stratosphere. Using the topographic concept, assuming that all water vapour is concentrated in the troposphere and that the water vapour content up to the tropopause is high enough for full absorption, a water vapour image reflects the height of the tropopause. In that way, the upper level potential vorticity distribution should match the structure of the water vapour image.

Mismatches between the model potential vorticity distribution and the water vapour image can indicate errors in either the model analysis or the forecast. Nowadays, techniques are being developed to improve the forecast by manually adjusting potential vorticity values to the water vapour structure and rerunning the model (a.o. [10, 16]). To make a good adjustment of the upper level potential vorticity field to the water vapour image, it is of great importance that their relationship is well known. As mentioned above, the correspondence is qualitatively understood, but it is not a one-to-one relationship ([10],[13]).

The motivation of this master's thesis is to further improve the understanding of the relationship between potential vorticity and water vapour images. To do so, we will develop a simple model based on radiative transfer (using the Schwarzschild equation), that is able to calculate a profile of the intensity of the radiation (radiance), or its conversion into a brightness temperature, in the water vapour absorption band from model input. We will include the absorption by water vapour and assume that clouds are absent. For the validation of the model we will use a more sophisticated model, Modtran4. The value at the top of the atmosphere can be compared to the radiance measured by a satellite in the water vapour channel. From its calculations for several gridpoints within a certain area, we can construct a synthetic water vapour image. Those model water vapour images can be directly compared to the model potential vorticity field. With the simple radiative transfer model, we will be able to understand what a water vapour image really tells us. We will investigate the exact influence of the humidity profile on the brightness temperature at the top of the atmosphere. Furthermore, we will examine the basic assumption that up to the tropopause enough water vapour is present for full absorption.

First, in Chapter 2, some theoretical aspects will be discussed. We will have a look at the distribution of potential vorticity in the troposphere and stratosphere, in relation to cyclogenesis. Besides, some remarks will be made on the interpretation of water vapour images. Furthermore, the link between the potential vorticity distribution and structures in water vapour imagery will be given a closer look.

Chapter 3 deals with the radiative transfer model we will develop. It starts with an introduction to an alternative method to construct water vapour images from model data developed by Tijm [15], from which one gets a first impression of the effect of absorption on the brightness temperature profile. Regarding the radiative transfer model, some theoretical aspects of radiative transfer are given, along with the numerical approximation and the validation by the reference model Modtran4. For a couple of HIRLAM gridpoints, calculations of brightness temperature profiles will be extensively discussed.

In Chapter 4, synthetic water vapour images are presented and compared with a real water vapour image. Regarding the relation between potential vorticity and water vapour images, the temperature at the dynamic tropopause (the surface where the potential vorticity has the value of 2 PVU) will be presented too. We will pay attention to the differences between using HIRLAM analyses as input and HIRLAM forecasts. Furthermore, a qualitative illustration of the relationship between potential vorticity and water vapour imagery will be presented, by overlaying the synthetic images with potential vorticity fields.

We will come back to the method by Tijm in Chapter 5. First, we will present an improvement of his method. Subsequently, we will prove that, although Tijm did not develop his method on the basis of radiative transfer theory, it can be related to radiative transfer theory. For that purpose, we will present both Tijm's method and the equation concerning radiative transfer in a form that clarifies their relationship.

Finally, Chapter 6 presents the conclusions and recommendations.

Chapter 2

Theory

2.1 Potential vorticity

Assuming hydrostatic equilibrium and taking the potential temperature θ as the vertical coordinate, the potential vorticity is given by:

$$P = -g(f + \zeta_\theta)\frac{\partial \theta}{\partial p}, \tag{2.1}$$

in which g is the acceleration due to gravity, f is the Coriolis parameter or planetary vorticity ($2\Omega \sin\phi$, Ω is the angular velocity of the earth and ϕ is the latitude), ζ_θ is the isentropic relative vorticity, i.e. the relative vorticity evaluated keeping the potential temperature θ constant, and p is the pressure. The unit of potential vorticity is PVU, where 1 PVU=$10^{-6}\mathrm{m^2s^{-1}Kkg^{-1}}$. Potential vorticity is the product of the absolute vorticity on an isentropic surface ($f + \zeta_\theta$) and the static stability ($-\partial\theta/\partial p$). In a standard atmosphere, the static stability increases only little with height in the troposphere and increases sharply in the stratosphere. So, in the stratosphere, potential vorticity values are much higher than in the troposphere. In general, the dynamic tropopause is given by the 2 PVU surface.

The advantages of the potential vorticity concept to describe and understand dynamic processes in the atmosphere, lie in two main properties of potential vorticity, its conservation and invertibility [6]. Potential vorticity is materially conserved if frictional and diabatic effects are neglected. This is valid for short time intervals and for airflows away from the earth's surface and clouds [4]. As a result, potential vorticity can serve as a label for air parcels. Once an air parcel is identified by its potential vorticity value, it can be followed in space and time. For example, intrusions of stratospheric air into the troposphere can be detected. If besides hydrostatic equilibrium also geostrophic equilibrium holds, potential vorticity is invertible. That means that from the potential vorticity field, all other fields, such as wind, temperature and pressure, can be derived.

Potential vorticity anomalies, such as upper level positive potential vorticity anomalies associated with a local lowering of the tropopause (i.e. bringing stratospheric air down to lower levels), influence the existing circulation and temperature patterns. As is described below, upper level positive potential vorticity anomalies enhance cyclogenesis. Hoskins et

al. [6] describe this potential vorticity approach to cyclogenesis, which is illustrated in Fig. 2.1. A local depression of the tropopause is advected over a low level baroclinic zone.

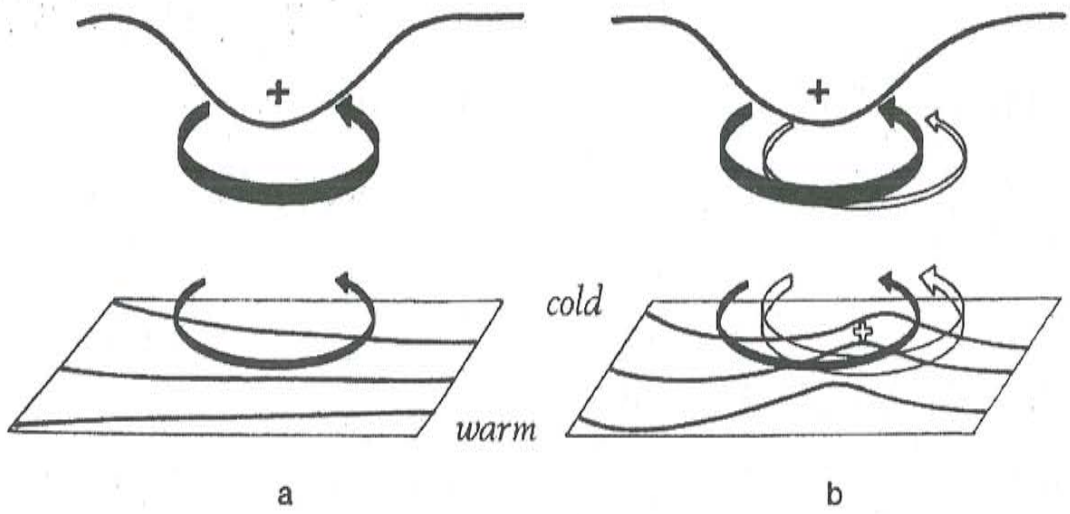

Figure 2.1: *A schematic picture of cyclogenesis associated with the arrival of an upper air potential vorticity anomaly over a low level baroclinic region. In (a), the upper air positive potential vorticity anomaly is represented by the solid plus sign. The induced cyclonic circulation is given by the solid arrows. Potential temperature contours are shown at the surface. In (b), the open plus sign represents the low level warm anomaly and the open arrows show the cyclonic circulation induced by the warm anomaly. From [6]*

The tropopause depression is accompanied by a positive vorticity anomaly. In geostrophic equilibrium, this implies a cyclonic velocity field. So, the upper level potential vorticity anomaly induces a cyclonic vortex that may extend all the way down to the surface. This is favoured by a large horizontal scale of the anomaly and low static stability. If it reaches the surface, it causes low level thermal advection that leads to a low level warm anomaly slightly east of the upper level potential vorticity anomaly. This positive potential temperature anomaly will induce its own cyclonic vortex that in turn may influence the wind field up to the tropopause. Because of the phase difference between the anomalies, the vortex induced at the surface causes an equatorward movement of the upper level potential vorticity anomaly. This leads to a decrease of the planetary vorticity contribution f to the absolute vorticity $(f + \zeta_\theta)$. In order to satisfy the conservation of potential vorticity, the relative vorticity ζ must increase, assuming that the static stability does not change. So, the cyclonic vortex induced by the upper level potential vorticity anomaly becomes even more cyclonic. In turn, potential temperature advection and thus the low level induced vortex, are enhanced. This positive feedback mechanism works as long as there is a phase difference between the anomalies. When the upper level anomaly catches up with the low level anomaly, no further intensification takes place and the system starts to decay.

2.2 Water vapour satellite imagery

The amount of radiation that travels in a certain direction is called the radiation intensity, or in short radiance. It is expressed in units of $Wm^{-2}sr^{-1}$. In the water vapour channel, the satellite measures the upwelling radiation emitted by the earth's surface and the atmosphere in a wavelength interval centered around 6.3 μm (5.7-7.1μm). In this interval, radiation is strongly absorbed and re-emitted by water vapour in the atmosphere. Since radiation from the lower troposphere is fully absorbed by the water vapour at higher levels, the satellite only receives radiation from the upper troposphere. In general, the layer between 200 and 600 hPa contributes most to the measured radiation [13]. If the atmosphere is moist, radiation is mostly received from the top layers. In a dry atmosphere, the radiation originates from lower layers because the dry layers above absorb radiation less.

In infrared bands, the radiance is highly correlated with the temperature of the emitting substance or object. Therefore, the measured radiance can be converted into a temperature, called the brightness temperature. This is the temperature of a black body that emits the same radiance in the same wavelength interval. Since the temperature in the troposphere decreases with altitude, the grey shades on a water vapour image more or less reflect the height of the layer that emitted the radiation. The next table gives some clues about the interpretation of different shades of grey [14]:

grey shades	**phase/content**	**indication of**
bright	liquid water	high clouds
grey values	water vapour	water vapour with varying content
dark	very low water vapour	dry upper and middle troposphere

There are factors that complicate the interpretation of water vapour imagery [13]. First of all, as is already evident from the table above, clouds also absorb and emit radiation in the water vapour channel. Unless clouds are very thin and high, only radiation above the cloud layer reaches the satellite. This accounts for the bright grey shades in water vapour imagery.

Furthermore, the upper troposphere is not a single layer with one humidity value. Moisture and clouds are distributed in several layers. This affects the brightness temperature. At low tropospheric levels, the temperature at which radiation is emitted is higher than at high levels. So the amount of radiation emitted is high, but almost all is absorbed by the water vapour in the atmosphere above it and very little reaches the satellite. At high levels, the transmittance of radiation to the satellite is high, but the amount of radiation is low, because of the lower temperature. These two conflicting effects combine in such a way that moist levels at some intermediate height contribute most to the measured radiation. Weldon and Holmes [17] called this the cross-over effect. It is important to keep in mind that the brightness temperature measured by the satellite is a "net" temperature of some layers of moisture, not the temperature of any single surface or layer. However, in water vapour satellite image interpretation a concept is often used that states that a water vapour image reflects the altitude of the top of a moist layer. This is called the topographic concept. It can be applied under the following conditions [17]: There are no clouds. Moisture is present up to a specific altitude, above which the air is relatively dry. This moisture is not arranged

in layers at altitudes above 600 hPa. And the air temperature decreases with altitude (there are no inversions). Under these circumstances, a water vapour image reflects the altitude of the top of the moist layer.

Finally, we need to take into account that the horizontal resolution of a geostationary satellite like Meteosat, decreases with latitude.

2.3 Potential vorticity in relation to water vapour imagery

If we adhere to the topographic concept and if we assume that water vapour is only present in the troposphere, a water vapour image reflects the height of the tropopause. Dark grey shades on the water vapour image tell us that the upper troposphere is dry. This can be interpreted as a lowering of the tropopause that brings dry stratospheric air down to levels that contribute to the radiance measured by the satellite. Since potential vorticity in stratospheric air is higher than in tropospheric air, dark values in the image should coincide with upper level positive potential vorticity anomalies. On the other hand, bright grey shades reflect a moist upper troposphere and should match negative upper level potential vorticity anomalies. We will now have a closer look at two features in water vapour imagery that are related to upper level positive potential vorticity anomalies.

2.3.1 Isolated tropopause depression

The cyclogenesis mechanism described in Section 2.1 is based on an isolated tropopause depression that causes an upper level positive potential vorticity anomaly. This idealized lowering of the tropopause is shown in Fig. 2.2. At the top of the figure, an indication of the representation of the tropopause depression by a water vapour image is given. We would see an almost circular or lens shaped region with dark grey shades. Such a dry region is called a "dry water vapour eye".

2.3.2 Tropopause folding

Another striking feature in water vapour imagery is a sharp boundary between dry and moist air as a result of tropopause folding. In a baroclinic region (as near the polar front), a circular dry water vapour eye will stretch out to a dry slot due to deformation of the background flow and descent of air along sloping isentropic surfaces [13]. Both stratospheric and upper tropospheric air experience adiabatic descent and as a result become warmer and drier. Grey shades on a water vapour image will therefore become darker. Since the isentropic surfaces slope in a baroclinic atmosphere, air will descend in a slantwise manner. This is schematically represented in Fig. 2.3. The intrusion of dry air is sandwiched by moister tropospheric air above and below. Descent of stratospheric air within a dry intrusion leads to tropopause folding. As can be seen from Fig. 2.3, in water vapour imagery tropopause folding can be recognized as a sharp transition from dark to bright shades. This also indicates the position

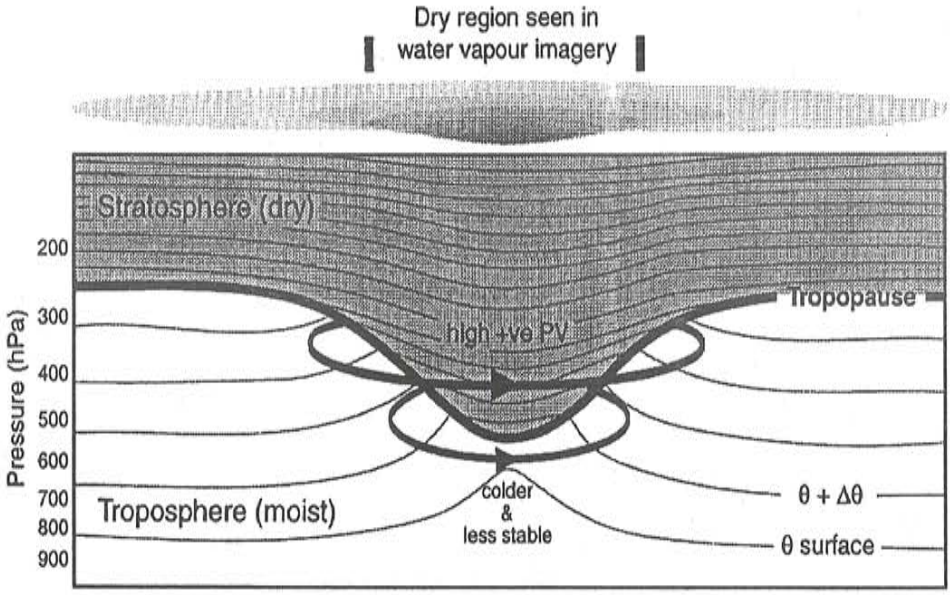

Figure 2.2: *An idealized model of a tropopause depression based on calculations performed by Thorpe (1985). The thick line is the tropopause, thin lines are isentropic surfaces. The lines with the arrows indicate the vorticity associated with the tropopause depression. From [13]*

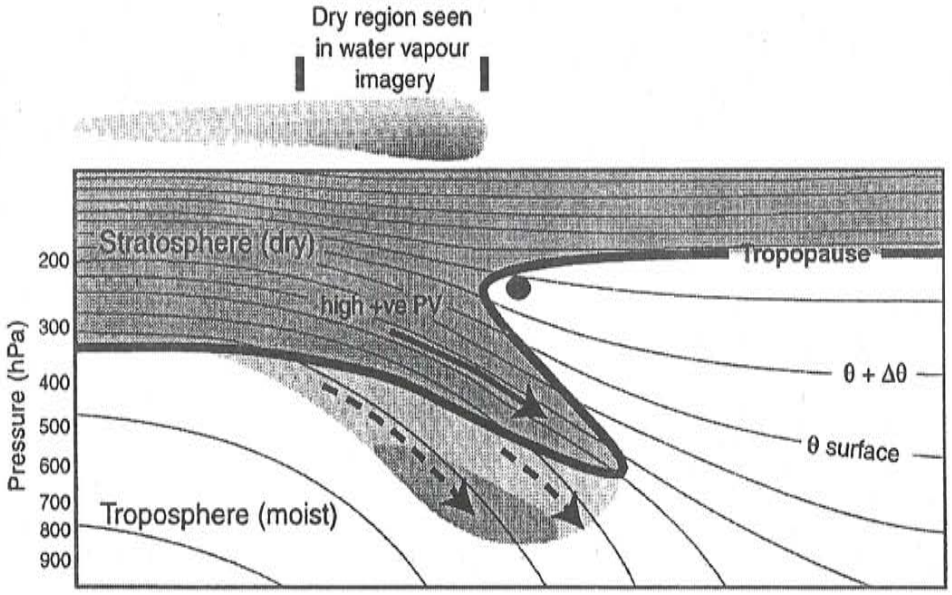

Figure 2.3: *Schematic diagram of a tropopause fold. The thick line is the tropopause, thin lines are isentropic surfaces. The continuous arrow shows stratospheric descent and dashed arrows show tropospheric descent. The black spot is an indication of the location of the jet stream in the baroclinic region. From [13]*

of the jet stream that is present in the upper troposphere within a baroclinic zone. In Fig. 2.3, the jet stream is located near the black spot, going into the paper.

Chapter 3

Radiative transfer model

A water vapour image represents the radiance in the water vapour channel measured at the top of the atmosphere. The radiance can be calculated by radiative transfer models. These models are based on the theory of the transfer of radiation through the atmosphere and include mechanisms like emission, absorption and scattering. They are being used in both weather and climate models. Absorption and scattering of radiation by gases, clouds and aerosols has great impact on the climate. However, the context of our study is more limited: we are interested in the relation between water vapour imagery and the dynamics of the atmosphere and will look at the absorption and emission by water vapour only.

In this chapter, we will develop and use a simple radiative transfer model that calculates from model data the brightness temperature in the water vapour channel (centered around 6.3 μm) at different levels in a vertical air column. For reasons of simplicity, we do not account for the absorption by clouds. The model is based on an analytical model developed at KNMI by Van Reenen [12]. The input to our model comes from the HIRLAM model [7] from which data of pressure, temperature and specific humidity is available at 31 levels. However, for the calculation of the profile at one specific gridpoint, we will only use the lowest 26 levels, from the earth's surface up to near 100 hPa. The data of the atmospheric layer above 100 hPa is not taken into account, because the water vapour content is too low to absorb upwelling radiation. The output will be compared to the brightness temperature profiles calculated by the radiative transfer model Modtran4 [2].

A method to construct synthetic water vapour images has already been developed at KNMI by Tijm [15]. Before we discuss our simple radiative transfer model, we will pay attention to Tijm's method, from which one gets a first impression of what happens with upwelling radiation if it is absorbed by water vapour.

3.1 Tijm's method

Tijm's method is developed in an intuitive way, without dealing with equations that concern radiative transfer. In Chapter 5, we will come back to this method and show that it can be related to the radiative transfer equation. In Tijm's method, the upwelling radiation from the earth's surface is followed on its way through the atmosphere. At the surface, which is assumed to emit as a black body, the brightness temperature is equal to the surface

temperature. If we go up one level and there is no water vapour present in that layer, the radiation will pass the layer unchanged, because no radiation is absorbed. So the brightness temperature stays the same. It will only change if the layer contains water vapour that absorbs the upwelling radiation. The higher the specific humidity in a layer, the higher the absorption of radiation by water vapour. The absorbed radiation will subsequently be emitted at the temperature of the absorbing layer. So, if all radiation coming from below is absorbed by a moist layer, the brightness temperature at the top of the layer gets the same value as the air temperature in the layer. If not all radiation is absorbed, the brightness temperature is given an intermediate value, depending on the fraction that is absorbed.

To determine this intermediate value, a threshold value for the specific humidity times the thickness (pressure difference) of the layer is implemented in the model. If it is exceeded, there is total absorption and the brightness temperature takes over the value of the air temperature. If the specific humidity times the thickness of the layer is only a fraction of the threshold value, the adaptation of the brightness temperature is only the same fraction of the difference between the air temperature in the layer and the brightness temperature at the previous level. This is summarized by the following equation [15]:

$$T_B = T_{B,old}\left(1 - MIN\left[1, \left(\frac{q\Delta p}{q_{wv}}\right)\right]\right) + T_a\left(MIN\left[1, \left(\frac{q\Delta p}{q_{wv}}\right)\right]\right). \tag{3.1}$$

T_B is the brightness temperature to be calculated at a specific level at the top of a layer, whereas $T_{B,old}$ is the calculated brightness temperature at the previous level. q is the specific humidity, Δp the thickness of the layer, q_{wv} the threshold value for the product of q and Δp and T_a the air temperature in the layer. MIN means that the minimum of the two numbers between brackets has to be taken. The threshold value q_{wv} is set to 3.0 Pa, because this value gave the best fit with real water vapour imagery [15].

Eq. (3.1) is evaluated at each level, starting at the surface level and going up to the top level near 100 hPa, resulting in a vertical profile of the brightness temperature. The value at the top level can be compared with the radiance measured in the water vapour channel of a satellite. An example is given in Fig. 3.1. For a certain HIRLAM gridpoint at the North Sea at the 23rd of April 2003 09 UTC (which is a +9h forecast), from now on referred to as "point 1", the profile of the brightness temperature is calculated. In the lower atmosphere, there is enough water vapour for total absorption, so the brightness temperature is equal to the air temperature. Above 700 hPa, the specific humidity times the pressure difference has dropped beneath the threshold value and only little absorption occurs. As a result, the brightness temperature does not decrease much anymore.

We will next present our radiative transfer model, starting with the theory of radiative transfer.

3.2 The model

As part of an undergraduate project, Van Reenen [12] developed a model to calculate the upwelling radiance in the water vapour channel, based on radiative transfer theory. An introduction to radiative transfer is given below. For details we refer to Van Reenen's report [12].

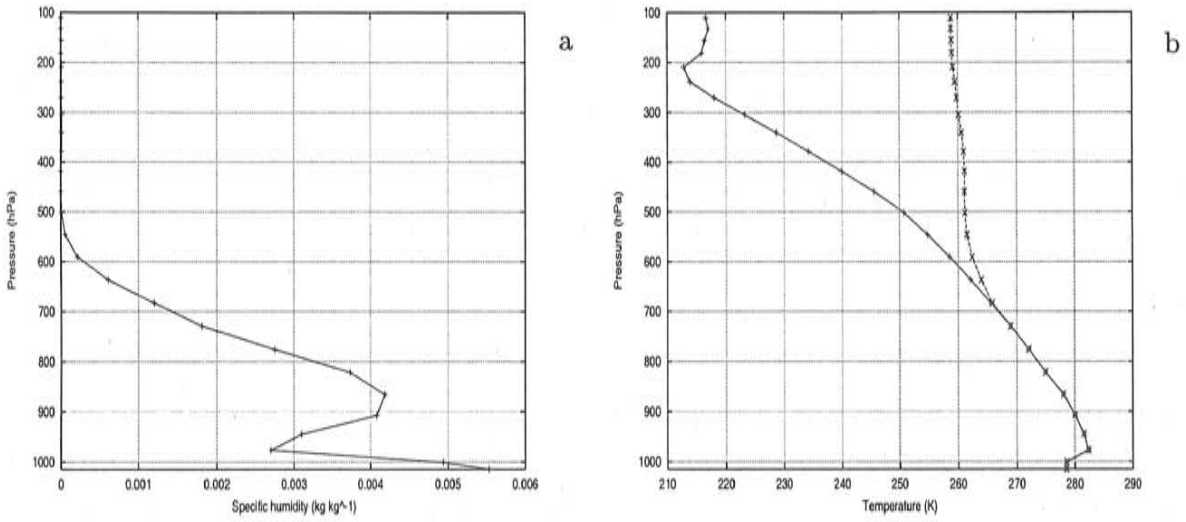

Figure 3.1: *Profile of (a) the specific humidity and (b) the air temperature (+) and the brightness temperature (X) for point 1, as calculated with the Tijm model.*

3.2.1 Radiative transfer theory

A black body is an object or volume element that absorbs all radiation. By Planck's law, the spectral radiance emitted by a black body is [9]:

$$B_\nu(T) = \frac{2hc^2\nu^3}{(e^{hc\nu/kT} - 1)}, \tag{3.2}$$

where T is the temperature of the object or volume element concerned, h is the Planck constant, c is the velocity of light, k is the Boltzmann constant and ν is the wavenumber (the reciprocal of the radiation's wavelength λ):

$$\nu = \frac{1}{\lambda}. \tag{3.3}$$

The B stands for black body radiation, which is the maximum amount of radiation a body with temperature T can emit. Spectral radiance is expressed in $\mathrm{Wm^{-2}sr^{-1}(cm^{-1})^{-1}}$.

Radiation that travels through the atmosphere is absorbed by clouds and gases. Although the water vapour content in the atmosphere is relatively small, it is an important absorber of radiation in the near-infrared and thermal infrared spectrum. We are interested in the absorption at 6.3 μm (1590 $\mathrm{cm^{-1}}$). Let us look at the attenuation due to absorption by water vapour of the spectral radiance I_ν, for radiation that originates at the earth's surface and travels vertically upward over a distance dz. This is given by the Beer-Bouguer-Lambert law [9]:

$$dI_\nu(z) = -I_\nu(z)k_\nu(z)\rho_v(z)dz, \tag{3.4}$$

where ρ_v is the density of water vapour and k_ν is the spectral absorption coefficient. Assuming hydrostatic equilibrium ($dp = -\rho g dz$), we can replace height by pressure as the vertical

coordinate:

$$dI_\nu(p) = I_\nu(p) k_\nu(p) \frac{\rho_v(p)}{\rho(p)} \frac{dp}{g}. \tag{3.5}$$

Introducing the specific humidity ($q = \frac{\rho_v}{\rho}$) and integrating the above equation, yields [12]:

$$I_\nu(p) = I_\nu(p^*) \exp\left\{ \frac{1}{g} \int_{p^*}^{p} k_\nu(p') q(p') dp' \right\}, \tag{3.6}$$

where p^* is the pressure at the earth's surface and p is the pressure at some level up in the atmosphere. The spectral radiance decreases exponentially. The exponent is the integral of the product of the spectral absorption coefficient k_ν and the specific humidity q over the pressure interval of the layer through which the radiation travels upwards, divided by the gravitational acceleration g. Here, p' represents all pressure levels between p^* and p. This is schematically represented in Fig. 3.2.

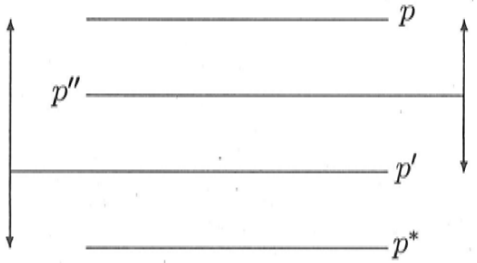

Figure 3.2: *Graphical scheme of the different pressure levels. p' from Eq. (3.6) varies between p^* and p and p'' from Eq. (3.7) varies between p' and p.*

The attenuation of radiation by absorption is often described in terms of the optical depth and the transmittance. The optical depth is a measure of the total absorption of the radiation traveling vertically upwards through an absorbing layer from a level p' to a level p. It is given by:

$$\tau_\nu(p', p) = -\frac{1}{g} \int_{p'}^{p} k_\nu(p'') q(p'') dp'', \tag{3.7a}$$

where p'' represents all pressure levels between p' and p. If we reverse the integration path, the minus will turn into a plus sign:

$$\tau_\nu(p', p) = \frac{1}{g} \int_{p}^{p'} k_\nu(p'') q(p'') dp''. \tag{3.7b}$$

The transmittance is a measure of the transmission of the radiation and is defined as the exponent of minus the optical depth:

$$\mathcal{T}_\nu(p', p) = e^{-\tau_\nu(p', p)}. \tag{3.8}$$

If no other absorption occurs above an absorbing layer, the optical depth at the top of that layer is zero and the transmission has the value of one. In that case all radiation emitted

from the top of the absorbing layer will reach outer space. The spectral absorption coefficient k_ν (expressed in m^2kg^{-1}) and the specific humidity q (kg kg^{-1}) determine the absorption within a layer.

The absorption by water vapour is not the only process that effects the spectral radiance. After absorbing upwelling radiation, water vapour will subsequently emit radiation of the same wavelength (Kirchhoff's law). If a volume of air is in thermodynamic equilibrium, the strenghtening of the vertically upwelling spectral radiance by emission by water vapour is given by [9]:

$$dI_\nu(z) = B_\nu(z)k_\nu(z)\rho_v(z)dz, \tag{3.9}$$

where B is the black body radiation from Planck's law.

If both absorption and emission by the atmosphere are included, Eqs. (3.4) and (3.9) combine to:

$$dI_\nu(z) = dI_{\nu,abs}(z) + dI_{\nu,em}(z) = -I_\nu(z)k_\nu(z)\rho_\nu(z)dz + B_\nu(z)k_\nu(z)\rho_\nu(z)dz. \tag{3.10}$$

This is the general equation for radiative transfer, called the Schwarzschild equation. In pressure coordinates, it may be written as:

$$dI_\nu(p) = \left(I_\nu(p) - B_\nu(p)\right) k_\nu(p)q(p)\frac{dp}{g}. \tag{3.11}$$

The Schwarzschild equation can be solved numerically in two different ways. The first is to integrate Eq. (3.11) directly, using a numerical integration method to obtain I_ν from a reference value at p^*. The second method is to use the formal solution of Eq. (3.11). Using the second method, we will be able to investigate from which part of the atmosphere the radiation comes from and what the magnitude of the contribution is. This is of vital importance in the understanding of a water vapour image. Therefore, we will now work with the formal solution of the Schwarzschild equation. In Chapter 5, we will come back to the direct numerical integration.

As can be checked straightforwardly, see [12], the formal solution, for an atmospheric layer from the surface p^* to a level p, is [9]:

$$I_\nu(p) = B_\nu(p^*)e^{-\tau_\nu(p^*,p)} + \frac{1}{g}\int_p^{p^*} k_\nu(p')q(p')B_\nu(p')e^{-\tau_\nu(p',p)}dp', \tag{3.12}$$

in which

$$\frac{1}{g}k_\nu(p')q(p')e^{-\tau_\nu(p',p)} = -\frac{\partial \mathcal{T}_\nu(p',p)}{\partial p'} = -\mathcal{W}_\nu(p',p). \tag{3.13}$$

$\mathcal{W}_\nu(p',p)$ is called the weighting function, the derivative of the transmittance. The first term in Eq. (3.12) is the surface contribution. It is the Planck function (Eq. (3.2)) at the surface times the transmittance of the total atmospheric layer. The atmospheric contribution, the

second term, is the integral over pressure of the Planck function times the weighting function. This product is referred to as the contribution function:

$$\mathcal{C}_\nu(p', p) = B_\nu(p')\mathcal{W}_\nu(p', p). \tag{3.14}$$

Taking into account the minus sign from Eq. (3.13), the formal solution may also be written as:

$$I_\nu(p) = B_\nu(p^*)e^{-\tau_\nu(p^*,p)} + \int_{p^*}^{p} \mathcal{C}_\nu(p', p)dp', \tag{3.15}$$

where the integration path has been changed with respect to Eq. (3.12).

To convert the spectral radiance I_ν into a brightness temperature, we will use the Planck function, Eq. (3.2). Recall that the brightness temperature is the temperature of a black body that emits the same radiance in the same wavenumber interval. We will restrict ourselves to a wavenumber interval that contains only a single wavenumber. If we substitute the black body radiation by the spectral radiance, we can obtain the brightness temperature T_B from

$$I_\nu = \frac{2hc^2\nu^3}{(e^{hc\nu/kT_B} - 1)}. \tag{3.16}$$

For the central wavenumber, 1590 cm^{-1}, the relation between the spectral radiance and the brightness temperature is shown in Fig. 3.3.

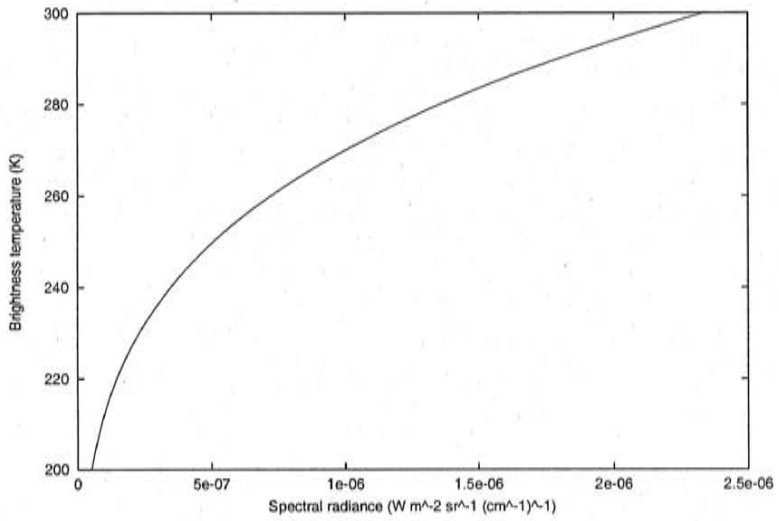

Figure 3.3: *Relation between the brightness temperature and the spectral radiance at 1590 cm^{-1} for the range of model output.*

Finally, we need an expression for the spectral absorption coefficient k_ν. It depends on the temperature, pressure and wavenumber. We will use an expression related to the one the Modtran3 radiative transfer model works with [8]:

$$k_\nu = C' \left(\frac{p}{p_0}\right)^n \left(\frac{T_0}{T}\right)^m, \tag{3.17}$$

where C' is a spectral parameter, p_0 is a reference pressure of 1000 hPa, T_0 is a reference temperature of 300 K an n and m are absorber parameters with values of respectively 0.9834 and -2.5294 for water vapour in a spectral range from 1005 to 1640 cm^{-1} [8]. In the original expression [8], the right part of Eq. (3.17) is raised to an absorber parameter a, that has a value of 0.5416. However, comparing our output with the Modtran4 model (see Section 3.2.3.2), we get the best results when a is 1. We treat C' as an adjustable parameter. In Section 3.2.3.2, we will deduce its value experimentally.

3.2.2 Numerical approximation

As $k_\nu(p)$ and $q(p)$ can be complicated functions of pressure, Eq. (3.12) cannot be integrated analytically, but has to be integrated numerically. The integral over pressure can be approximated by a sum over pressure intervals, using the trapezoidal approximation. In that way, the contribution of each interval to the total radiance is calculated and summed up. An integral is best approximated by small discretization intervals.

At an arbitrary number of levels, the radiance can be calculated. We will calculate the radiance profile at 26 levels, equidistant in pressure. The value represents the radiance that would be measured at that height, which is the sum of the contributions by all intervals between the evaluation level and the earth's surface, except for the surface level. There, the value represents the radiance emitted by the surface.

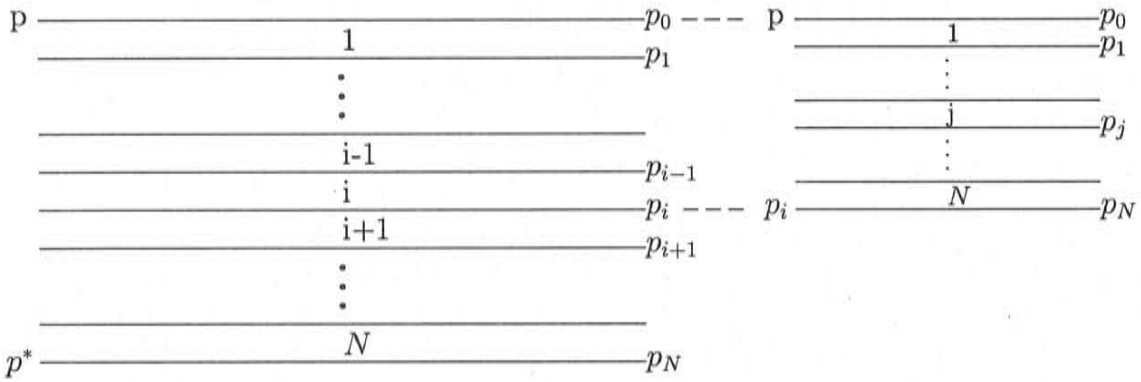

Figure 3.4: *Graphical scheme of the discretization of Eq. (3.12). The left scheme shows the discretization for the radiance as in Eq. (3.20), the right scheme shows the related discretization for the optical depth as in Eq. (3.22).* $N = 100$.

Fig. 3.4 shows the discretization scheme that is used in the numerical approximation of the formal solution of the Schwarzschild equation. The pressure at the discretization levels for the radiance is given by:

$$p_i = p_0 + i\Delta p_i, \quad i = 1, \ldots, N, \qquad with\ \Delta p_i = \frac{p^* - p}{N} \tag{3.18}$$

The pressure at the discretization levels for the optical depth is:

$$p_j = p_0 + j\Delta p_j, \quad j = 1, \ldots, N. \qquad with\ \Delta p_j = \frac{p_i - p}{N} \tag{3.19}$$

The numerical approximation of Eq. (3.12) is:

$$I_\nu(p) \cong B_\nu(p^*)e^{-\tau_\nu(p^*,p)} + \frac{1}{g}\sum_{i=1}^{N}\left(k_\nu q B_\nu e^{-\tau_\nu}\right)(i)\Delta p_i, \tag{3.20}$$

in which the integrand is the mean of the values at the top and the bottom of interval i:

$$\left(k_\nu q B_\nu e^{-\tau_\nu}\right)(i) = \left(k_\nu(p_i)q(p_i)B_\nu(p_i)e^{-\tau_\nu(p_i,p)} + k_\nu(p_{i-1})q(p_{i-1})B_\nu(p_{i-1})e^{-\tau_\nu(p_{i-1},p)}\right)/2. \tag{3.21}$$

p is the evaluation level, the level for which the radiance will be computed. N is the number of discretization intervals with thickness Δp_i and p_i is the pressure at the lower boundary of interval i, referred to as discretization level. For every evaluation level p in Eq. (3.20), we will use N intervals, so these are not fixed intervals.

The optical depth, Eq. (3.7b), is approximated by:

$$\tau_\nu(p_i, p) \cong \sum_{j=1}^{N}(k_\nu q)(j)\frac{\Delta p_j}{g}. \tag{3.22}$$

For the numerical approximation of the optical depth, again N intervals are used. Note that these do not have thickness Δp_i, but Δp_j. For every discretization level p_i in Eq. (3.20), Δp_j is different, because we always use N intervals. As above, the integrand is the mean of the values at the top and the bottom of the interval j.

For N, we will take the value of 100. In the next section, we will illustrate why we work with this number of intervals for each numerical integration.

3.2.3 Validation

In order to derive a value for C' for Eq. (3.17) and to check the model output, we will compare it with output from the narrow band model Modtran4 [2]. We will use Modtran4 as a reference, since we did not find any observations of the profile of upwelling radiance in the water vapour absorption band. Before we will look at the results, we will first discuss whether the numerical approximation as described above, is adequate to calculate radiative transfer throughout the atmosphere.

In our study, we will use HIRLAM data for four gridpoints that have different humidity profiles. These points are:

number	location	forecast time
1	53.5N/5.0E (North Sea)	23rd of April 2003 09 UTC
2	53.0N/6.8E (North Netherlands)	23rd of April 2003 09 UTC
3	44N/3W (Bay of Biscay)	17th of March 2003, 09 UTC
4	37N/4W (South Spain)	17th of March 2003, 09 UTC

Point 1 is the same HIRLAM gridpoint as the example in Section 3.1.

3.2.3.1 Validation of the numerical approximation

Being proportional to the exponent of minus the optical depth, the amount of radiance is very sensitive to little changes in optical depth. The optical depth at the top of a moist layer is, by definition, zero. Using the trapezoidal approximation, the mean optical depth of the upper discretization interval will therefore be quite small, yielding a high radiance contribution. This effect is more pronounced in the lower atmosphere, because at the underlying levels the optical depth is greater in comparison with the higher atmosphere due to higher water vapour content. In the lower atmosphere the humidity is in general high enough for full absorption and so most radiation comes from the upper discretization interval. Since the calculation uses the mean optical depth of the upper and lower boundary of the discretization interval, one can imagine the impact of the optical depth being zero at the top of the upper discretization interval. As a result, the radiance will be overestimated in the lower atmosphere. It turns out that the radiance in the lower atmosphere is best approximated using many thin intervals.

It is also valuable to work with variable intervals. From a programming point of view, it is easy to use a fixed number for every separate numerical summation, both of the radiance as of the optical depth, independent of the level for which the radiance will be computed. Besides the practical advantage of easy programming, this implies also that in the lower atmosphere, the thickness of the intervals is very small, preventing the overestimation of the radiance mentioned before. Another advantage is that the optical depth is approximated most accurately for the upper discretization level (p_1 in Fig. 3.4). For the lower atmosphere this is advantageous, because the upper discretization interval contributes most to the total radiance. However, for the upper atmosphere this does not hold, because above a certain pressure level, depending on the humidity profile, it is no longer the upper interval that contributes most. Recall the cross-over effect, mentioned in Chapter 2.

We will work with that number of intervals, that will give a good approximation of the radiance profile (compared to the Modtran4 model, see Section 3.2.3.2) and at the same time will not require too much computation time. We found this number to be 100. Working with 100 intervals, will satisfactory solve the problem mentioned above in the lower atmosphere. This can clearly be seen in Fig. 3.5, where we vary the number of intervals and compare the output with Modtran4. 200 intervals would be even better, but the improvement does not compensate for the increase in computation time.

In our study, we will use temperature and humidity data from the HIRLAM model to calculate a radiance profile. As mentioned earlier, data of pressure, temperature and specific humidity are available at 26 levels, from the earth's surface (level 26) up to near 100 hPa (level 1). Since we will work with variable intervals, interpolation must be applied in order to get the values at the discretization levels. We will use linear interpolation for that purpose.

3.2.3.2 Validation of the output by Modtran4

Modtran is a narrow band model, which means that it works with narrow spectral bands for which the spectral characteristics are averaged. Its name is deduced from MODerate resolution TRANsmittance code. Modtran4 is an upgrade that has spectral bands of 1 cm^{-1} [2]. The spectral radiance as computed by our simple radiative transfer model, can be compared with the Modtran4 monochromatic radiance in the interval 1589.5-1590.5 cm^{-1},

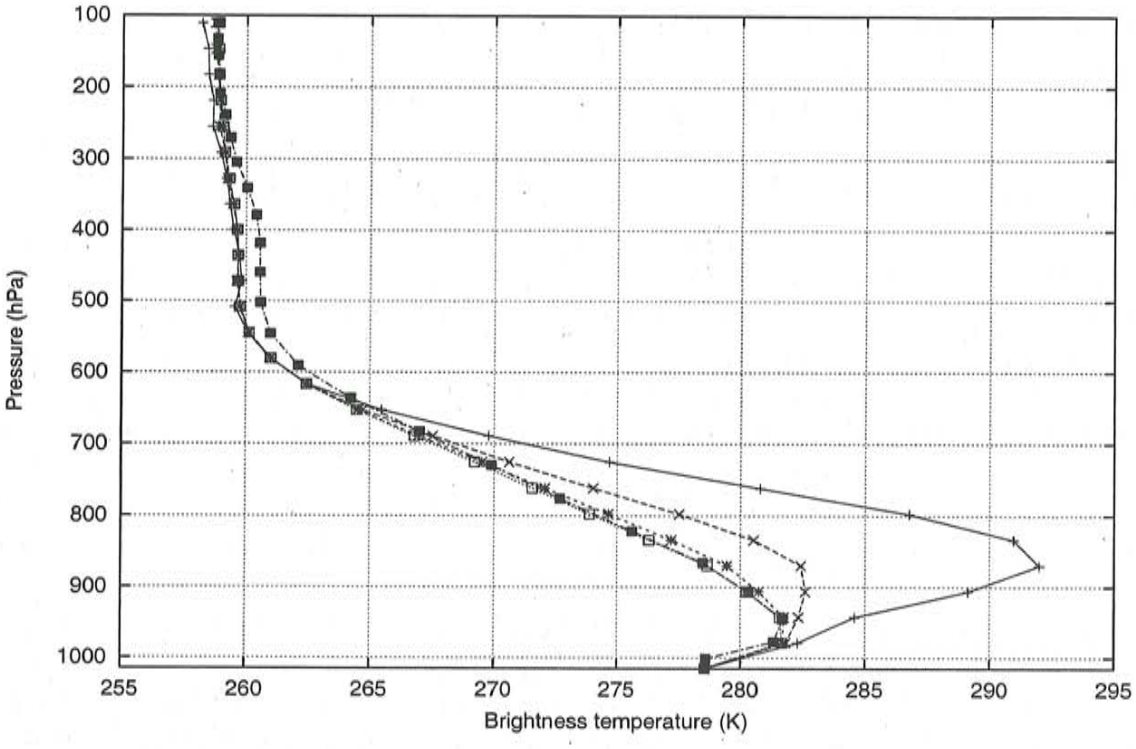

Figure 3.5: *Profile of the brightness temperature for 25(+), 50(X), 100(*) and 200(□) intervals, in comparison with the Modtran4 profile (black squares), for point 1.*

with central wavenumber 1590 cm^{-1}, if all other absorbing gases, clouds and aerosols within Modtran4 are set to zero. The Modtran4 monochromatic output is treated as the reference profile, from which we derive the value for C'. By experiment, we found that the value of 14.0 m^2kg^{-1} gives the best fit with Modtran4 output.

Fig. 3.6 shows the profiles for some grid points, that will also be looked at in Section 3.3, computed by both Tijm's method and the simple radiative transfer model, next to the output of Modtran4. The air temperature is plotted too, to show that the brightness temperature stays equal to the air temperature in the lower atmosphere as long as there is sufficient water vapour present to fully absorb the upwelling radiation. At first sight, both Tijm's method and the simple radiative transfer model, show good correspondence with Modtran4. If we look a bit closer, at the output for the top of the atmosphere, the radiative transfer model fits to Modtran4 for all four points. Tijm's method shows a small deviation for point 2 and a large deviation for point 4. These points have the lowest brightness temperatures, so the method seems to overestimate the absorption in the upper troposphere. In Chapter 5, we will relate Tijm's method to radiative transfer theory and improve the method, in such a way that the output at the top of the atmosphere will be in close agreement with the output of the radiative transfer model.

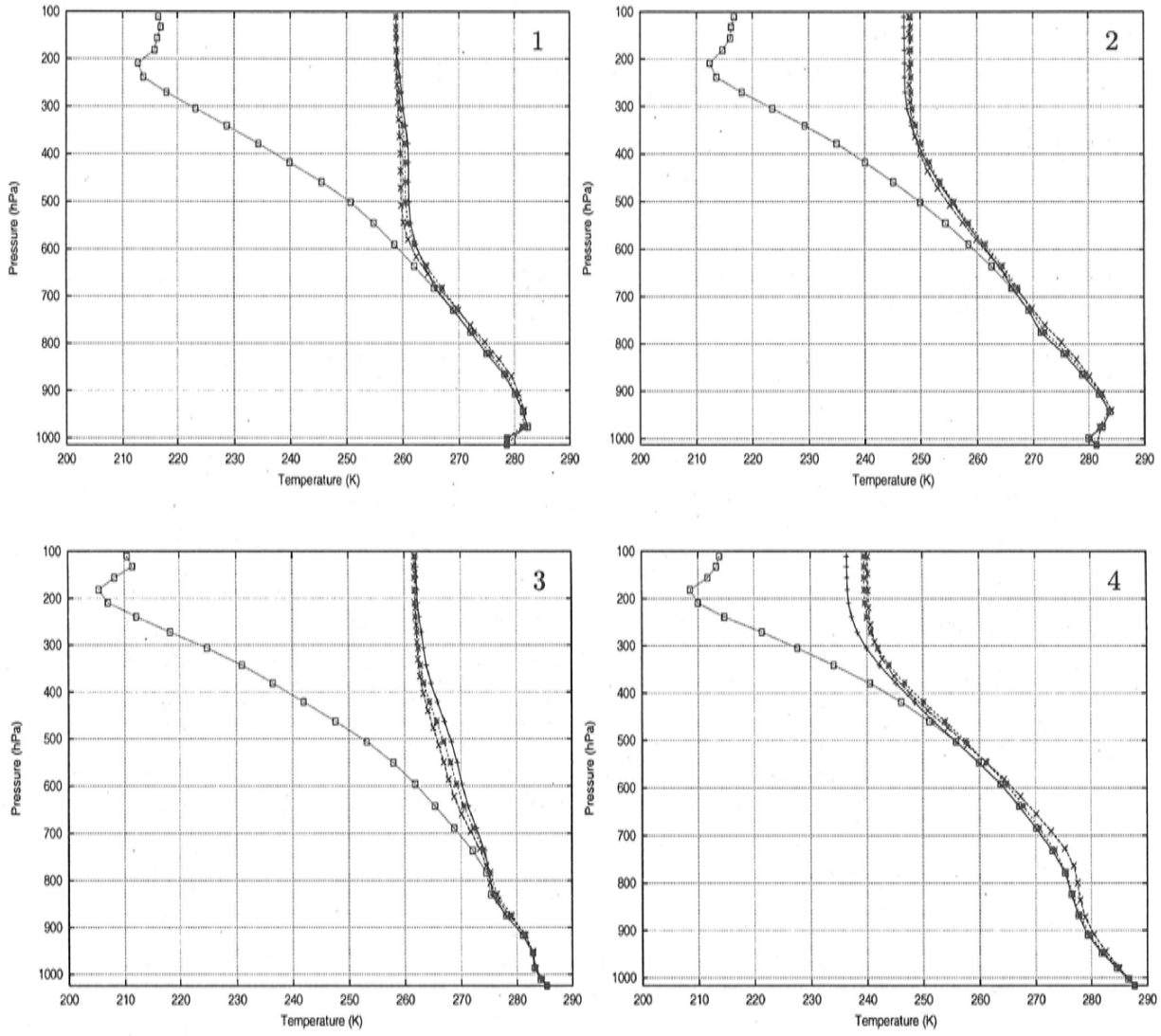

Figure 3.6: *Brightness temperature profiles by Tijm's method (+), the radiative transfer model (X) and the reference model Modtran4(*) for points 1,2,3 and 4, along with the air temperature (□).*

The radiance at the top of the atmosphere is measured by satellites in specific bandwidths and converted into a brightness temperature. In order to be able to compare our output of the brightness temperature at the top of the atmosphere with real water vapour images, we would like to know the total radiance at the top within the satellite wavenumber interval (the so-called bandwidth). The (first generation) Meteosat water vapour channel has a bandwidth of 1400-1750 cm^{-1}. The total radiance is obtained by integrating the monochromatic radiance over this interval. For simplicity, we will assume that the monochromatic radiance at the central wavenumber, $\overline{\nu}$ (1590 cm^{-1}), is representative of all wavenumbers in the interval. In that case the total radiance is obtained by multiplying the monochromatic radiance by the bandwidth $\Delta\nu$:

$$I(p) = \int_{\Delta\nu} I_\nu(p)d\nu \cong \Delta\nu I_{\overline{\nu}}(p). \tag{3.23}$$

The conversion of the total radiance into a brightness temperature comes down to dividing the total radiance by the bandwidth and applying Eq. (3.16) where ν is $\overline{\nu}$. So, in our case there is no difference in using the total radiance or the monochromatic radiance in calculating the brightness temperature.

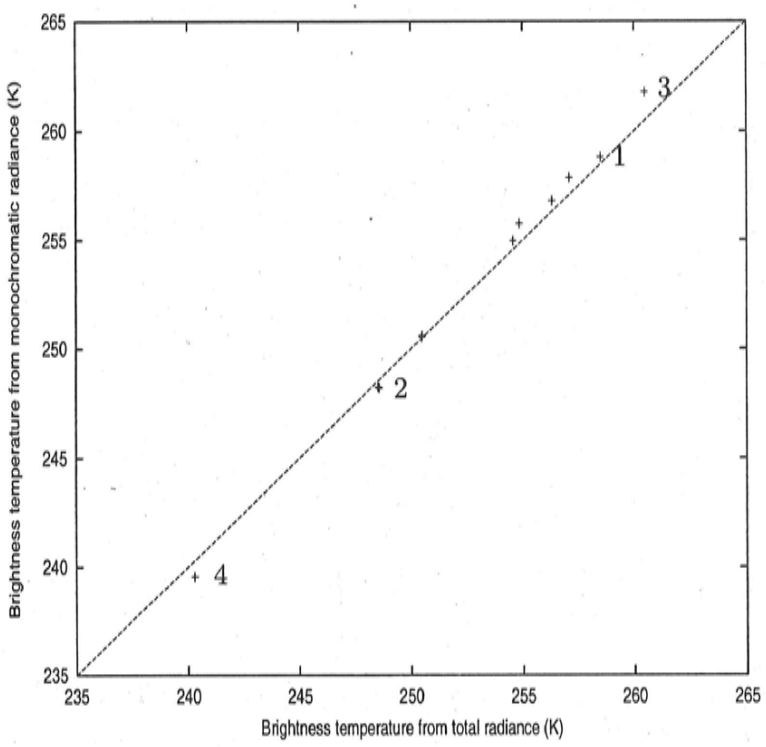

Figure 3.7: *The values of the brightness temperatures at the top of the atmosphere, as deduced from the Modtran4 total radiance against those deduced from the Modtran4 monochromatic radiance. If equal, the points will be situated at the straight line.*

In Modtran4, spectral variability within the bandwidth is taken into account. The total radiance is the sum of the radiances of all spectral intervals with central wavenumbers from

1400 to 1750 cm^{-1}. We will apply the same conversion into the brightness temperature as in our model. The difference between taking the total radiance and the monochromatic radiance in Modtran4 is shown in Fig. 3.7. Next to points 1, 2, 3 and 4 (see Section 3.3), we will plot another 7 gridpoints, from which we have the HIRLAM profiles, to make it more significant. The maximum difference is -1.3 K at point 3. We consider the differences small enough to justify the assumption of spectral homogeneity within the bandwidth, that we made in our simple radiative transfer model.

3.3 Results

As already mentioned in Section 3.2.3.1, we will use four gridpoints to illustrate the results of our calculations of brightness temperature profiles. The air temperature profiles of these gridpoints have already been presented in Section 3.2.3.2, Fig. 3.6.

3.3.1 Profiles of humidity and brightness temperature

Figs. 3.8 and 3.9 present the specific humidity and computed brightness temperature profiles. It is evident that higher specific humidity values give a lower brightness temperature at the top of the atmosphere. This is because the higher the water vapour content is, the higher the absorption will be. Full absorption means that the brightness temperature equals that of the air temperature. Therefore, in the lower atmosphere the profile of the brightness temperature follows that of the air temperature (see also Fig. 3.6, Section 3.2.3.2). When the humidity becomes lower, absorption will decrease and eventually no absorption will take place. From that level, the brightness temperature stays the same. For point 4, this level lies highest, around 300 hPa, because its water vapour content is still high enough to absorb radiation in the upper atmosphere. The water vapour content of point 1 already decreases to a value of little to no absorption at 600 hPa. As a result, the brightness temperature at the top is much higher than that of point 4. The highest brightness temperature at the top is from point 3. This humidity profile shows low values all through the atmosphere, resulting in little absorption. Looking at the humidity profiles of points 1 and 2, at first sight they seem quite alike. However, since at point 2, water vapour is present higher in the atmosphere, which apparently is enough for absorption, the brightness temperature profiles show a large difference above 600 hPa.

3.3.2 Optical depth and radiance contribution

To obtain more insight into the construction of the brightness temperature profile, we will look at the optical depth and the atmospheric contribution to the total radiance by the discretization intervals. For point 1, Fig. 3.10 shows these quantities for the moist layers that go up to each evaluation level. Since the optical depth at the top of a moist layer is, by definition, zero, the height of the evaluation level (or top of the moist layer concerned) is given by the pressure at which the optical depth is zero. The line starting at the evaluation level, and going towards the earth's surface, represents the optical depth at different heights within the layer concerned. It is obvious that for every layer the optical depth is highest at

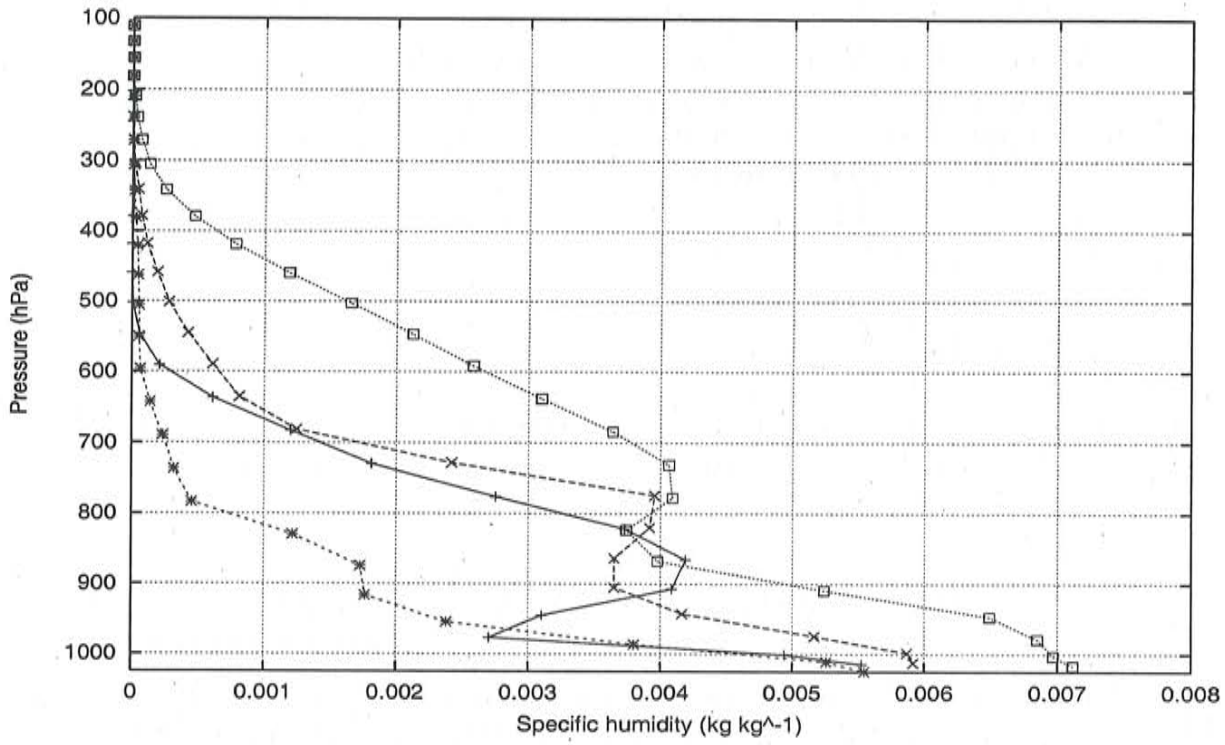

Figure 3.8: *Profiles of the specific humidity for points 1(+), 2(X), 3(*) and 4(□).*

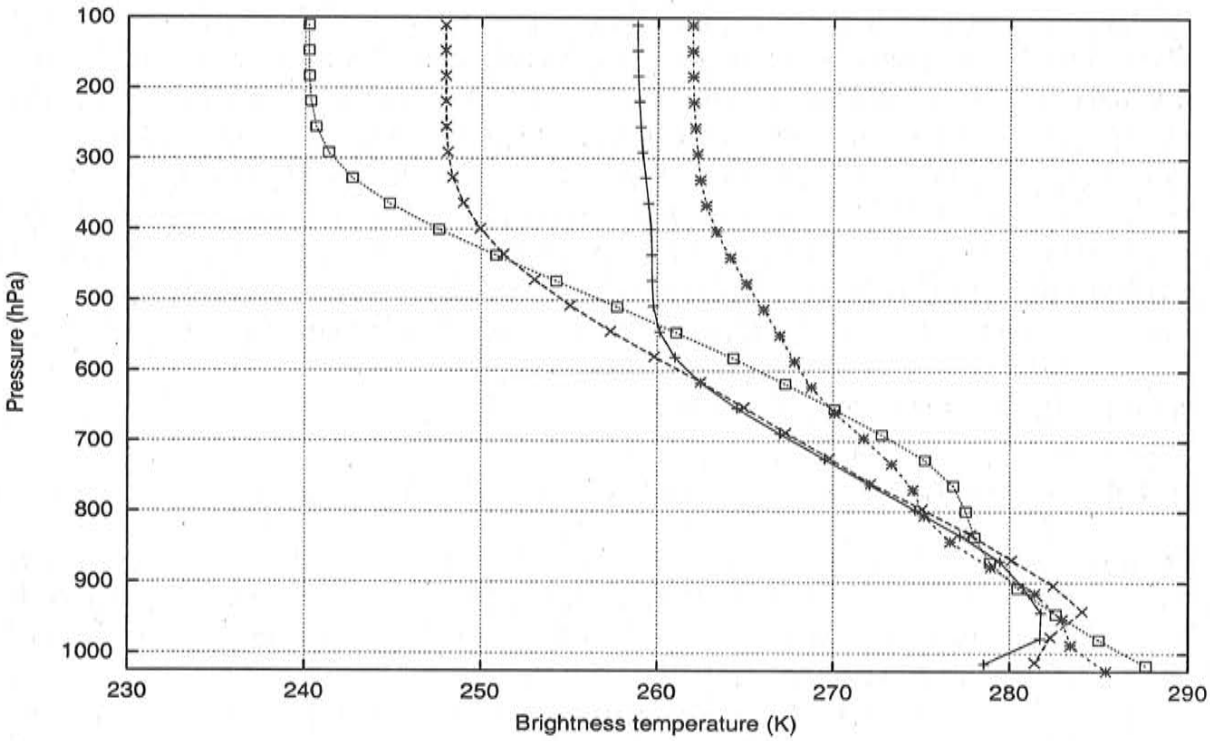

Figure 3.9: *Profiles of the brightness temperature for points 1(+), 2(X), 3(*) and 4(□).*

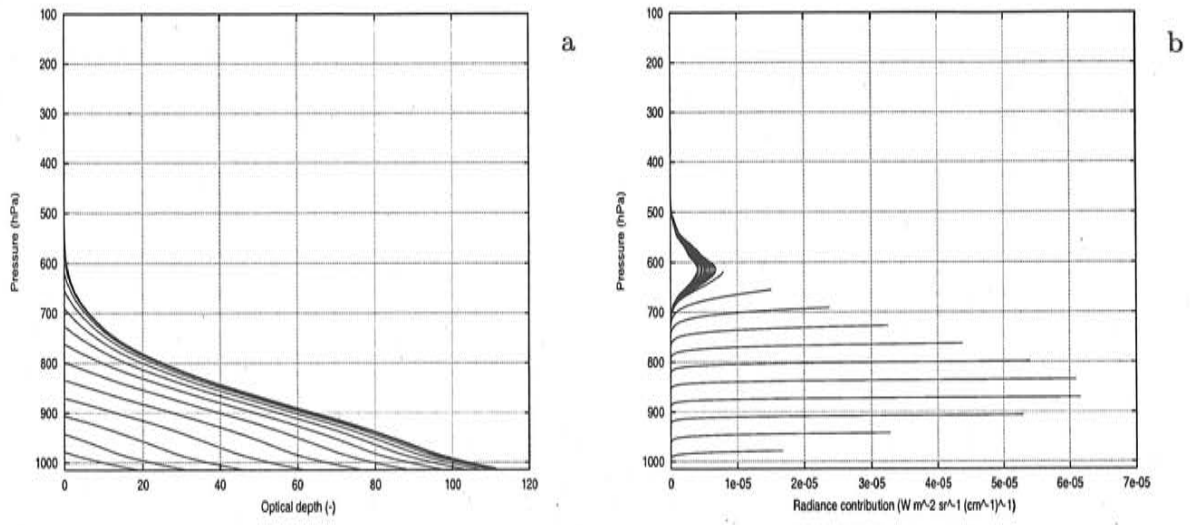

Figure 3.10: *The optical depth $\tau_\nu(p', p)$ (a) and contribution to the total radiance $C_\nu(p', p)dp'$ (b) for point 1. Each separate line belongs to the moist layer that goes from the surface up to the different evaluation levels. For practical reasons, a line is plotted, but actually this is the connection between the values at the 101 discretization levels.*

the surface. The optical depth of the whole moist layer that goes up to 800 hPa, is 87, but the upper part from 800 to 900 hPa has an optical depth of 40. With decreasing pressure of the evaluation level, the optical depth will increase. However, above 560 hPa, it does not change anymore. The water vapour content in the upper atmosphere is too low to further increase the optical depth. The same moist layers as in Fig. 3.10a, are plotted in Fig. 3.10b. The height of the evaluation level is now found at the end of the lines. The line represents the radiance contribution to the radiance that reaches the evaluation level, at different heights in the layer concerned. All lines start from the surface, where the atmospheric contribution is zero. If we look at the layers in the lower atmosphere, the ones that do not exceed 620 hPa, we see that only the upper part contributes. The contribution of the layers that do exceed 620 hPa, shows a maximum at 620 hPa. So, for these layers, most radiation comes from 620 hPa. Fig. 3.10b illustrates the point that we made in Section 3.2.3, that in the lower atmosphere, most radiation comes from the upper discretization interval. If we consider the whole atmosphere, the cross-over effect makes that moist layers near 620 hPa contribute most to the total radiance. Neglecting the contribution of the earth, which is very low even for the evaluation level just above the surface, the total radiance at each evaluation level is the sum over the contributions from the earth's surface up to the evaluation level. After converting the total radiance into the brightness temperature, the result is the profile we already showed in Fig. 3.9.

For all four points, the contribution to the total radiance at the top of the atmosphere at the discretization levels and the corresponding optical depth is given in Figs. 3.11 and 3.12. We can see clearly that the optical depth and the height of the intervals that contribute most to the total radiance at the top of the atmosphere depend on the humidity profile (Fig. 3.8). Intervals in the upper atmosphere that do not contain enough water vapour,

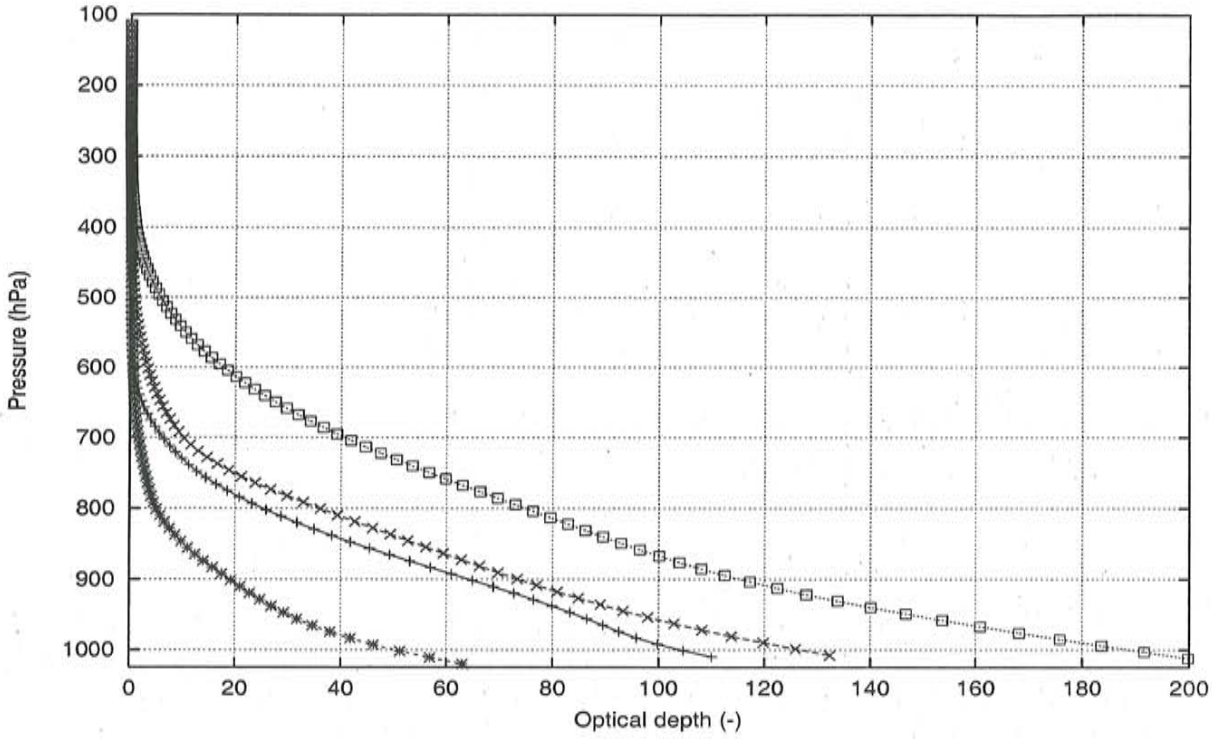

Figure 3.11: *The optical depth for the whole atmosphere for points 1(+), 2(X), 3(*) and 4(□).*

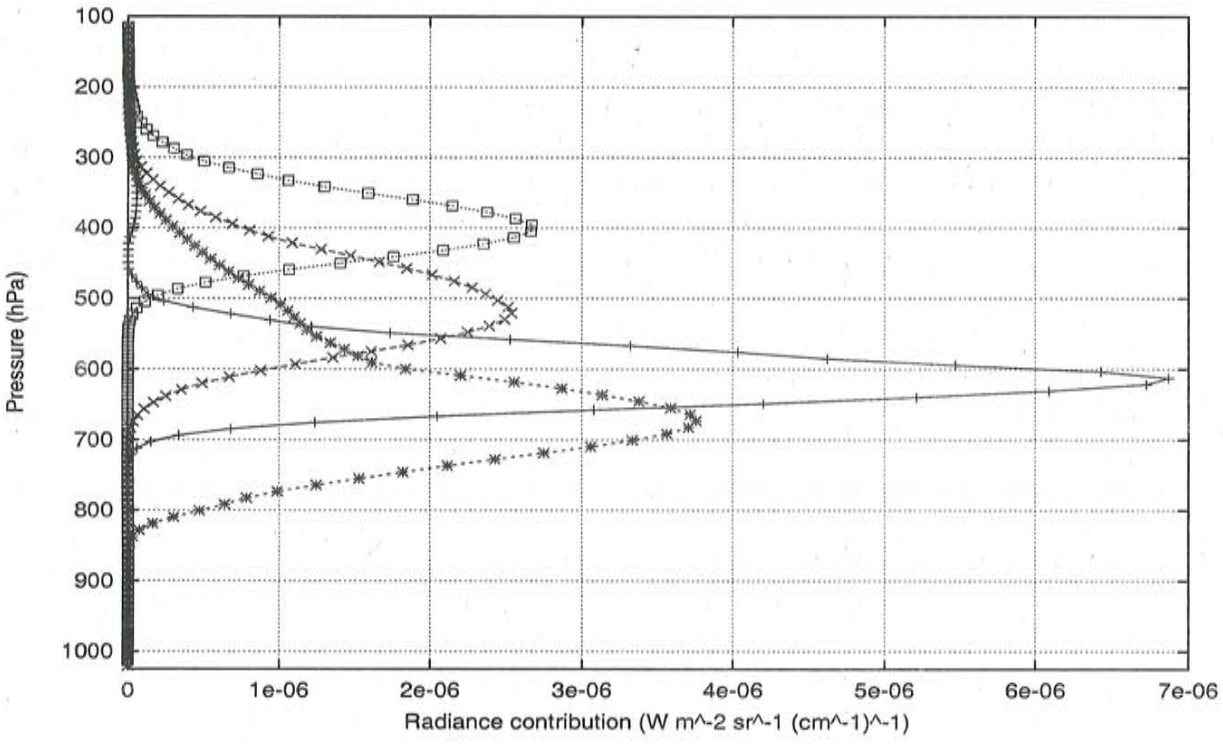

Figure 3.12: *The contribution to the radiance at the top of the atmosphere for points 1(+), 2(X), 3(*) and 4(□).*

do not contribute to the radiance. Also, if the optical depth is too large, the intervals do not contribute. All radiation that they emit is absorbed before it would reach the top of the atmosphere. In the upper atmosphere the optical depth is very small, so much of the radiation that reaches the top comes from this region. However, because of the lower temperatures, the amount of the radiance contribution is smaller than in the lower part of the atmosphere (the cross-over effect). In Fig. 3.12 we can see that the radiance of point 4, that has the highest humidity in the upper atmosphere, comes from the moist layer between 250 and 500 hPa. The height of maximum contribution of the other points, decreases with decreasing humidity. At the "dry" point 3 even radiation from as low as 800 hPa contributes to the radiance at the top. As is clear now, there are exceptions to the general rule that the layer between 200 and 600 hPa contributes most to the measured radiation at the top of the atmosphere [13]. Also, we can already call in question the assumption that up to the tropopause enough water vapour is present to have full absorption, and above the tropopause the air is completely dry. Referring to the topographic concept, mentioned in Section 2.2, this can still be applied because the brightness temperature at the top of the atmosphere gives an indication of the height of the contributing part of the atmosphere.

If we look at the maximum contribution of point 1 (around 620 hPa), it is much higher than the maximum of the other points. The reason fot this is that the water vapour content above the level of maximum contribution is very low, resulting in a high transmittance. Therefore, nearly all radiation coming from the maximum level can reach the top of the atmosphere. In order to substantiate this statement, we adapted the humidity profile of point 2, in such a way that up to 680 hPa it does not change and above that level, it takes over the values of point 1. Indeed, the contribution peak of the adapted point 2 showed the same shape and magnitude order as point 1. Of course, the magnitude of the contribution depends also on the specific humidity and temperature at the level of maximum contribution, but the water vapour content in the layer above is the most important factor.

3.3.3 Using fixed relative humidity profiles

On the whole, we can say that the vertical distribution of water vapour throughout the atmosphere is very important in the determination of the radiance at the top of the atmosphere. The higher the height at which significant water vapour is present in the atmosphere, the lower the brightness temperature will be. The humidity in the lower atmosphere does not matter if enough water vapour is present at higher levels. This is proved by applying our numerical model with temperature profiles from the HIRLAM model and assuming a constant relative humidity throughout the atmosphere. Appendix A describes the conversion of relative into specific humidity. The profiles of the specific humidity and the brightness temperature for point 1 are shown in Figs. 3.13 and 3.14. We see that if there is no water vapour at all (the relative humidity is 0%), no absorption takes place and the brightness temperature is equal to the surface temperature. A low relative humidity, 5%, already gives substantial absorption causing the profile of the brightness temperature to follow the air temperature profile in the lower atmosphere and resulting in a value of 260 K at the top of the atmosphere. Increasing the relative humidity makes the profile shift to lower brightness temperatures. The shift is not a linear function of the relative humidity. It decreases with

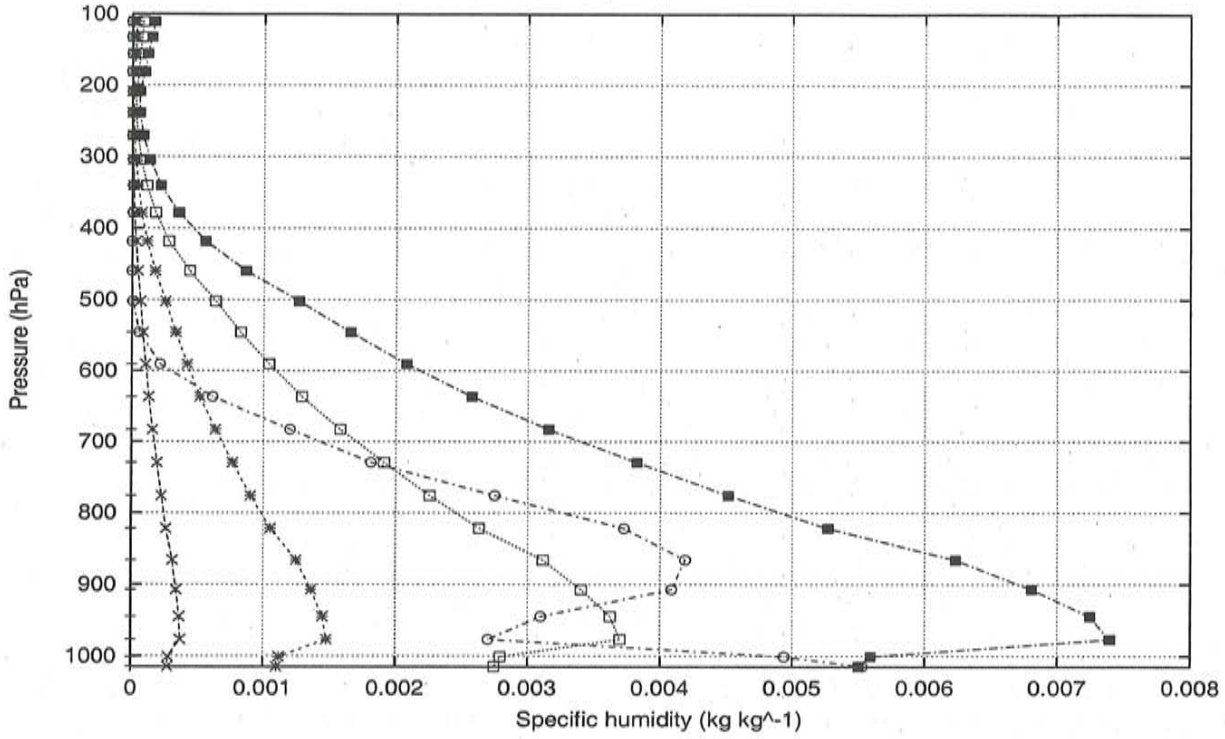

Figure 3.13: *The specific humidity profile of point 1(○), and the profiles if we work with different values of constant relative humidity: 0%(+), 5%(X), 20%(*), 50%(□) and 100%(black squares).*

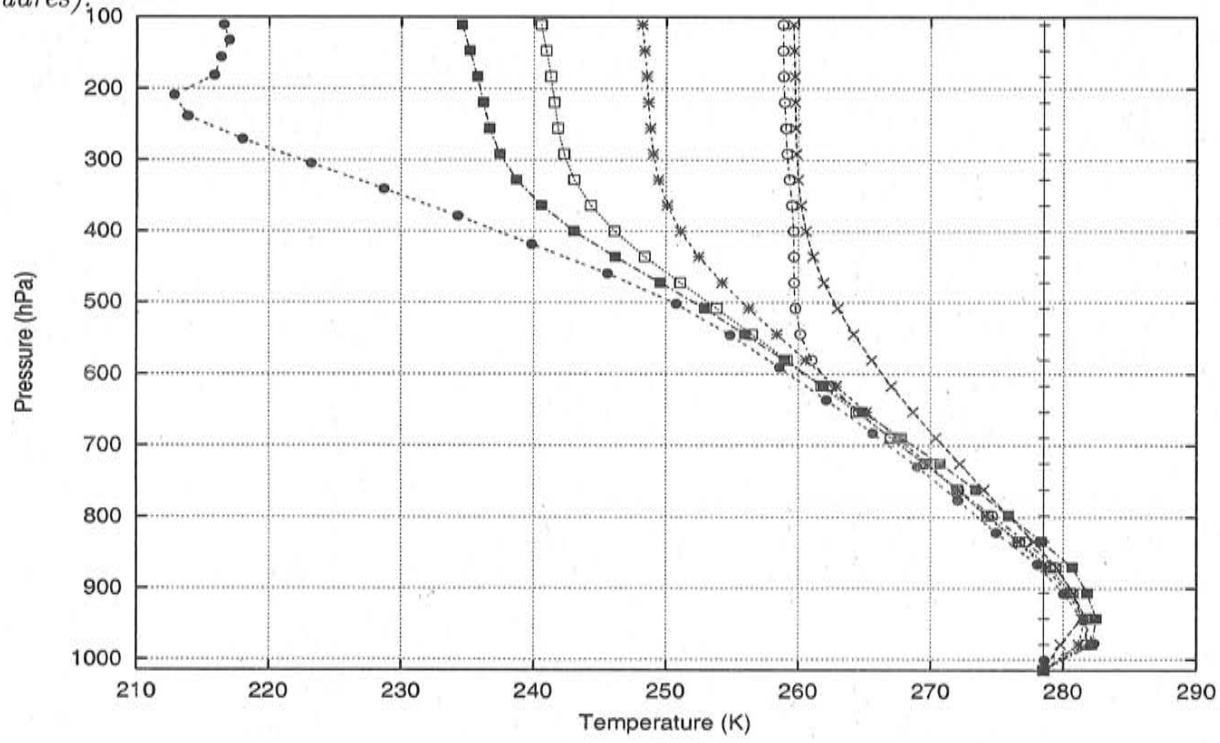

Figure 3.14: *The brightness temperature profiles corresponding to the humidity profiles in Fig. 3.13 and the air temperature(●).*

increasing relative humidity. The higher the relative humidity, the longer the brightness temperature stays (nearly) equal to the air temperature. Van Reenen's study [12] works with a constant relative humidity of 100% in the troposphere and 0% in the stratosphere. It is clear now that this is not realistic. The minimum value the brightness temperature can have, when the relative humidity is 100%, is 234 K. If we assume that the temperature decreases with height in the troposphere and increases with height in the stratosphere, the tropopause is situated around 200 hPa, where the temperature is 213 K. So even if the relative humidity in the troposphere would have been 100%, the water vapour image would not reflect the height of the tropopause. The water vapour content in the upper troposphere is not enough for full absorption (see also Fig. 3.15). As we will see in Chapter 4, this is true for even moister profiles.

In the lower atmosphere, the profiles of the brightness temperature for different relative humidity values, nearly overlap. So, the water vapour content in this part of the atmosphere does not have much influence on the brightness temperature at the top of the atmosphere. The vertical distribution of water vapour determines which part of the atmosphere contributes to the radiance that reaches the top of the atmosphere. Looking at Fig. 3.13 we see that around the level of maximum contribution, 620 hPa, the humidity is about 20%, and it decreases rapidly to nearly zero at 500 hPa. The resulting brightness temperature at the top corresponds to the value, the atmosphere would give if the relative humidity had a constant value of 6%. So, the humidity in the lower atmosphere, that lies around 50%, does not play any role.

Fig. 3.15 shows the contribution to the total radiance at the top of the atmosphere at the discretization levels for the profiles of 100%, 20% and 5% relative humidity. As a reference, the actual profile of point 1 is given too. It is clear that as the relative humidity decreases, the contribution to the radiance that reaches the top of the atmosphere, comes from lower in the atmosphere. We see that the reason that 5% relative humidity yields higher radiance at the top of the atmosphere than 20%, is that the contributing part of the atmosphere is thicker. As for 100%, it is clear that there is no full absorption up to the tropopause. Since the temperature increases with height above the tropopause, in this calculation there is even a contribution from the stratosphere, but this is not realistic. We should have put the water vapour content to zero, but it will not make much difference. Fig. 3.15 shows good correspondence with Fig. 1.1.11 from Bader et al.[1] that shows the approximate levels from which radiation in the water vapour channel reaches the satellite for relative humidity values of 100%, 50% and 25%.

3.3.4 Conclusion for vertical air columns

Concluding, the vertical distribution of water vapour throughout the atmosphere is very important in determining the radiance at the top of the atmosphere. Not only does it determine which part of the atmosphere contributes to the upwelling radiation that reaches the top of the atmosphere, but it also has great influence on the magnitude of the contribution.

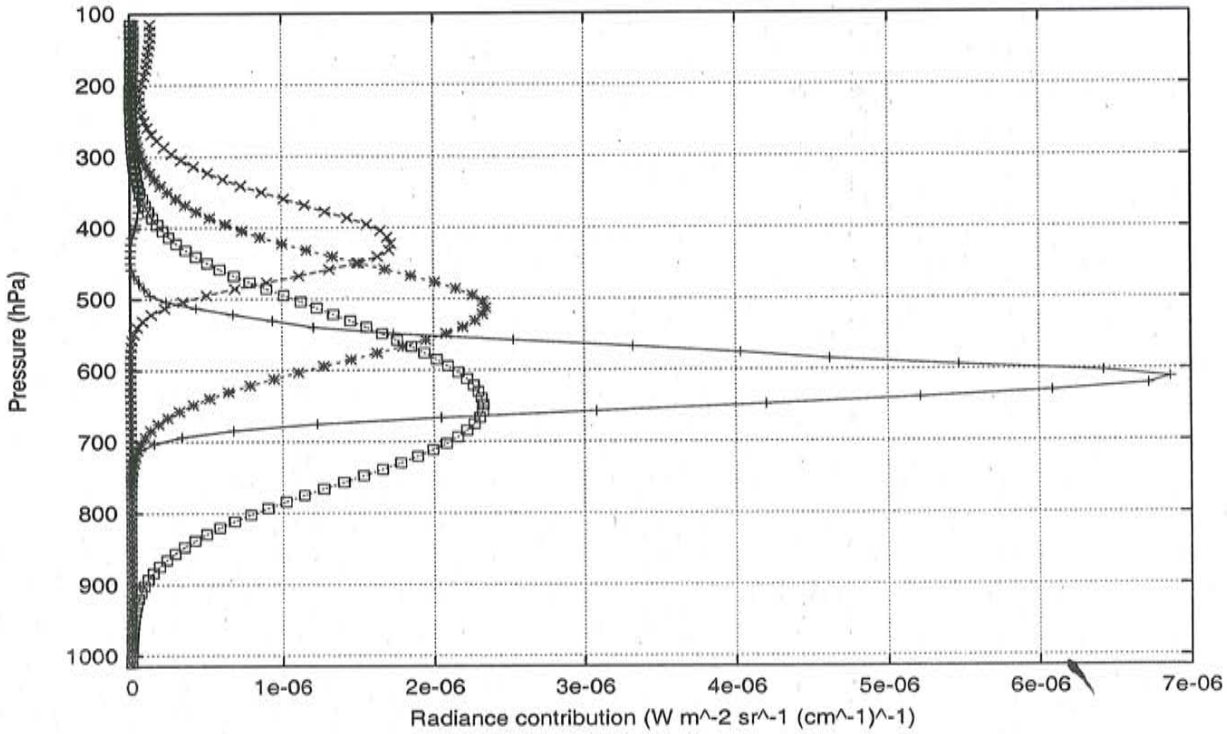

Figure 3.15: *The contribution to the radiance at the top of the atmosphere for the actual profile of point 1(+), the 100%(X), 20%(*) and 5%(□) relative humidity profiles.*

Chapter 4

Synthetic water vapour images

Using the simple radiative transfer model from the previous chapter, we will construct a synthetic water vapour image by calculating the brightness temperature at the top of the atmosphere for a field consisting of 164 x 130 gridpoints. However, only part of the field is looked at, namely the area of the North Atlantic and Europe. For programming convenience, we will now work with all 31 levels from the HIRLAM 55 km resolution model. In order to save computation time, we will work with 50 pressure intervals, instead of the 100 that are used in the calculation for single gridpoints in Chapter 3. As can be seen in Fig. 3.5, for the value at the top of the atmosphere, this does not make much difference.

If we want to compare our synthetic water vapour image with a real water vapour image from the Meteosat satellite, which is located 36000 km above the equator, we have to bear in mind that the satellite measures the intensity of the radiation that travels from a point at the surface up to the satellite's sensor and not of the radiation that travels upward perpendicular to the surface. However, in Appendix B, we will show that in the case of the HIRLAM 55 km resolution model, this difference may be neglected.

We will work with the case of the 29th of October 2002, 06 UTC. Fig. 4.1 shows the real water vapour image from Meteosat (first generation). The colour bar at the bottom of the water vapour image, gives the range of brightness temperature values in Kelvin. Above the North Atlantic Ocean, near the coast of Ireland a significant dark area can be seen in the water vapour image. It is situated at the rear of a boundary that lies over Scotland and Denmark, towards eastern Europe.

4.1 Analysis of the 29th of October 2002 06 UTC

In the first case, we will use the HIRLAM fields of the initialized synoptic analysis of the 29th of October 2002, 06 UTC as input.

4.1.1 Synthetic water vapour image

Fig. 4.2 shows the synthetic water vapour image. The synthetic image is plotted with the same grey shade scale as the real image in order to make a fair comparison. Comparing the synthetic water vapour image with the real water vapour image, we see that large structures

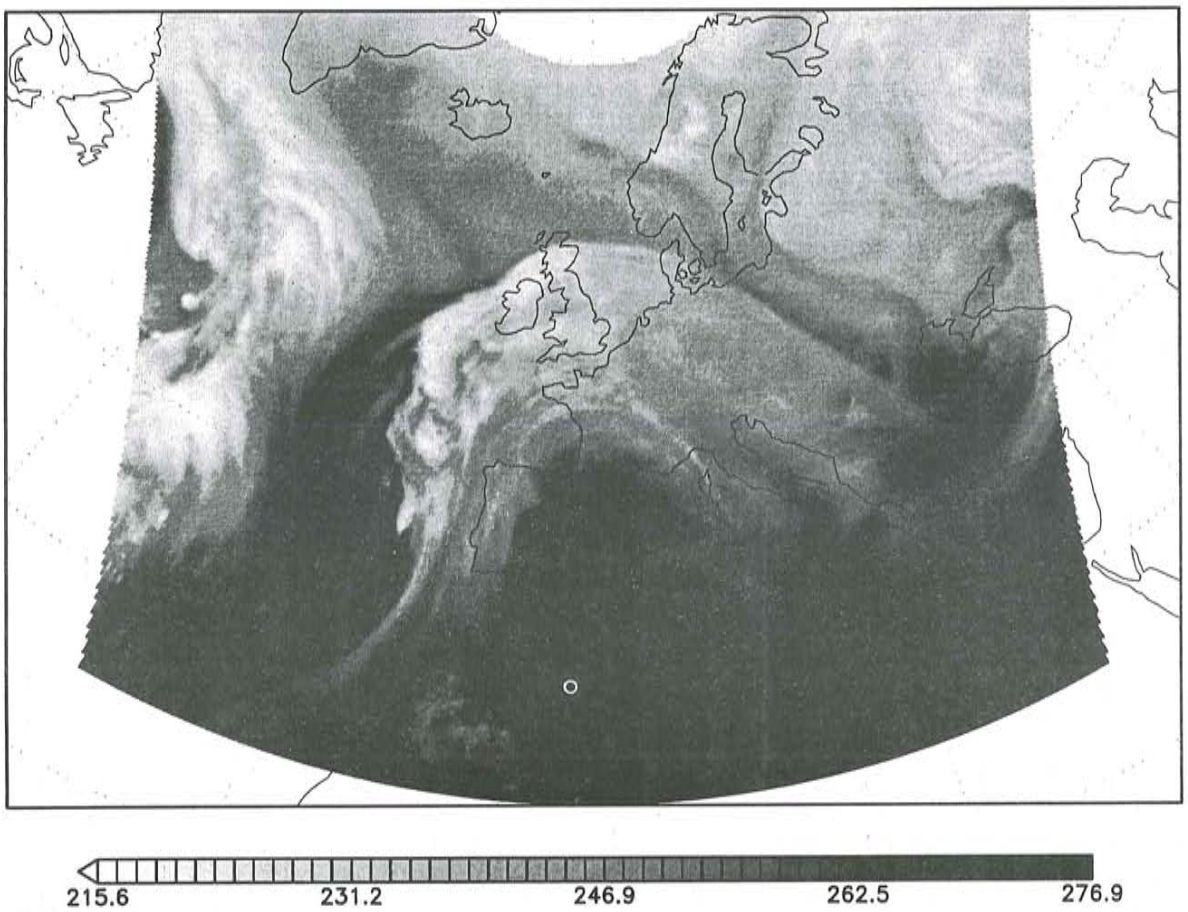

Figure 4.1: *The real water vapour image of the 29th of October 2002, 06 UTC (brightness temperature in Kelvin). The white circle presents the location of the station 60571, used in Fig. 4.3.*

are in agreement, except for the sharp boundary over eastern Europe towards the Black Sea. The bright white shades in the real image show high clouds, that are absent in the synthetic image, because we only account for the absorption by water vapour. So, in order to get more realistic images, we should also include the absorption by clouds in our model. This will be one of the most important recommendations we will make at the end of this report.

Another striking feature is the large dark area in the south of the real water vapour image. Our model seems to overestimate the absorption in this nearly subtropical region. This could lie in the fact that the humidity in the HIRLAM analysis is too high. However, comparing these values with humidity data from soundings at locations that lie in the dark area, shows that this is not the case. For a sounding from station 60571, situated at 31.5N;2.25W, as indicated by the white circle in Fig. 4.1, the brightness temperature profile is calculated and compared with the model profile. This is presented in Fig. 4.3. The sounding is from 00 UTC, but we also calculated the profile from the 12 UTC sounding, which showed comparable humidity and temperature values, except near the surface. The model air temperature profile is in good agreement with the temperature profile from the sounding, so differences in the

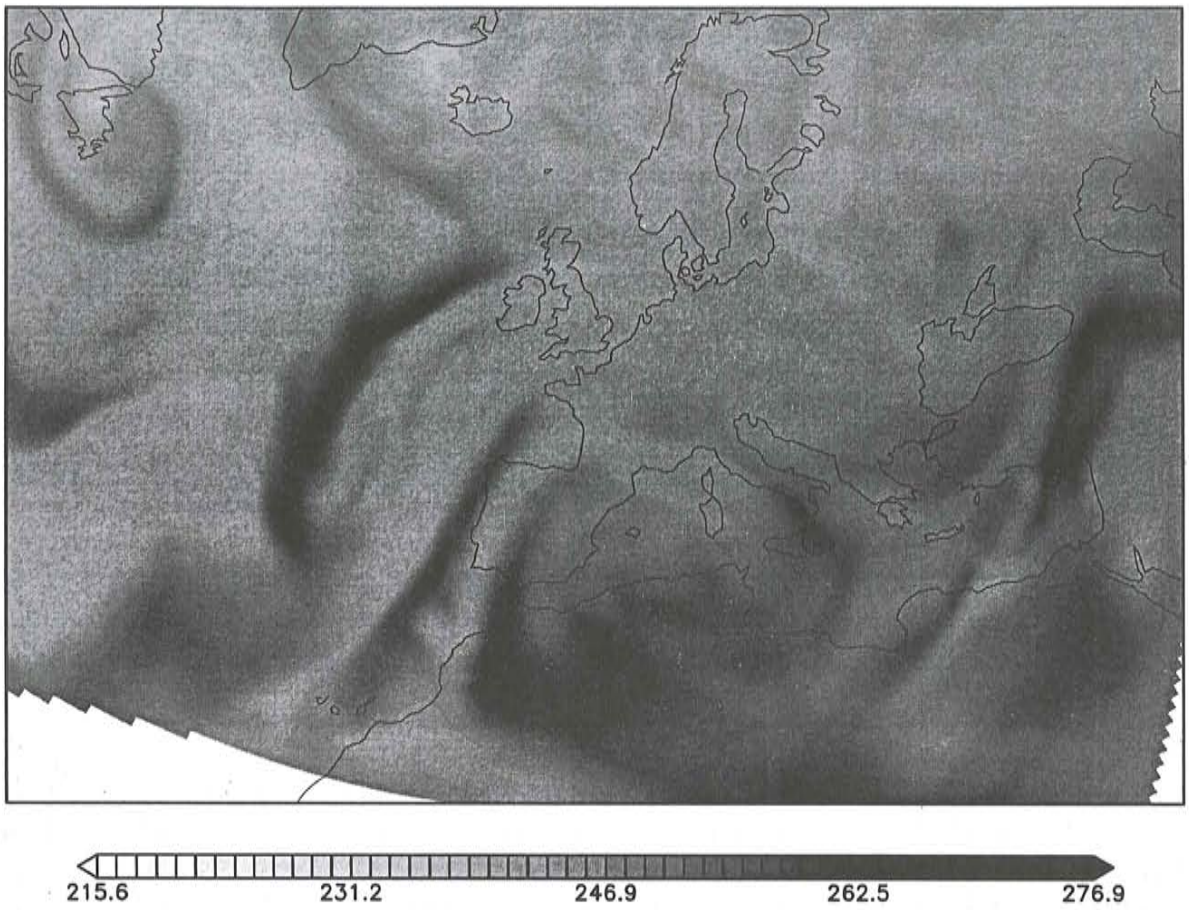

Figure 4.2: *The synthetic water vapour image of the analysis of the 29th of October 2002, 06 UTC (brightness temperature in Kelvin).*

brightness temperature are a result of the differing specific humidity profiles. At first sight, looking at Fig. 4.3a, the model humidity is not too high. It is evident that the sounding shows a lower brightness temperature profile, which is not what we expected from the dark grey shades in the real water vapour image. For comparison, the brightness temperature in the real water vapour image is higher than 275 K. We looked at several other stations but none of the sounding profiles showed much higher brightness temperatures. So, the humidity in the HIRLAM analysis is not too high in this region.

Another possible explanation may lie in the fact that at higher latitudes, the angle between the perpendicularly upward travelling radiation and the actual slant path towards the Meteosat satellite, is larger. We again refer to Appendix B. The radiative transfer model works with a fixed value for the gravitational acceleration g. However, if the radiation travels in a slantwise manner, we should actually correct g with $\cos\alpha$ in order to get the orthogonal projection of g on the actual path of the radiation (SM in Figs. B.1 and B.2). We did some experiments with this correction and it turned out that it reduces the brightness temperature at the top of the atmosphere. The higher the latitude, the higher the reduction is. So, although the brightness temperature becomes even lower, in the south the reduction

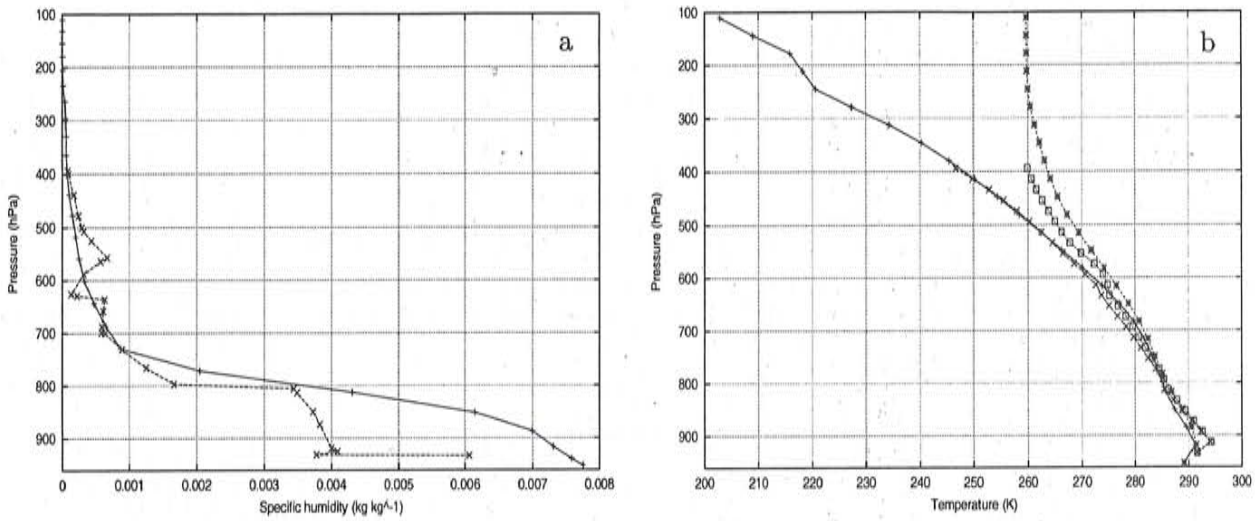

Figure 4.3: *For a location near 31.5N;2.25W, profiles of a) the specific humidity from HIRLAM(+) and the sounding(X) and b) the air temperature from HIRLAM(+) and the sounding(X) and the brightness temperature calculated from HIRLAM(*) and from the sounding(□).*

is less than in the north. However, differences are small. For 50N we found a reduction of around 4 K, for 31.5N the reduction was 2.5 K. As a reference, we also made calculations for slant paths with Modtran4, yielding differences of the same order. The difference is too small to explain the much darker area in the real water vapour image in comparison with the synthetic images. So, at this moment, we do not understand this feature of the real satellite image.

4.1.2 Temperature at the dynamic tropopause

In Section 3.3.3, we showed for point 1, that the troposphere does not contain enough water vapour for full absorption and it is not the temperature of the tropopause that is reflected in the water vapour image. We will show that this is valid for all humidity profiles in the area that is covered by HIRLAM. Fig. 4.4 shows the temperature at the dynamic tropopause (the 2 PVU surface), again with the same grey shade scale as the real water vapour image. Indeed, the grey shades are brighter than those of the real water vapour image, so the temperature at the tropopause is lower. However, we can see very clearly that large structures in the real water vapour image are also present in the tropopause temperature field. Moreover, the sharp boundary over eastern Europe towards the Black Sea, that is not shown by the synthetic water vapour image, is very obvious in Fig. 4.4. An explanation may lie in the fact that the synthetic water vapour image in Fig. 4.2 is based on an analysis. There are large areas, like eastern Europe, that have few observations from soundings. Therefore, the first guess of the analysis adapts only slightly to observations. The first guess of the dry dynamics like the tropopause temperature is likely to be better than the first guess of humidity. Therefore, sharp boundaries in humidity may not be represented in the analysis, whereas the analysis

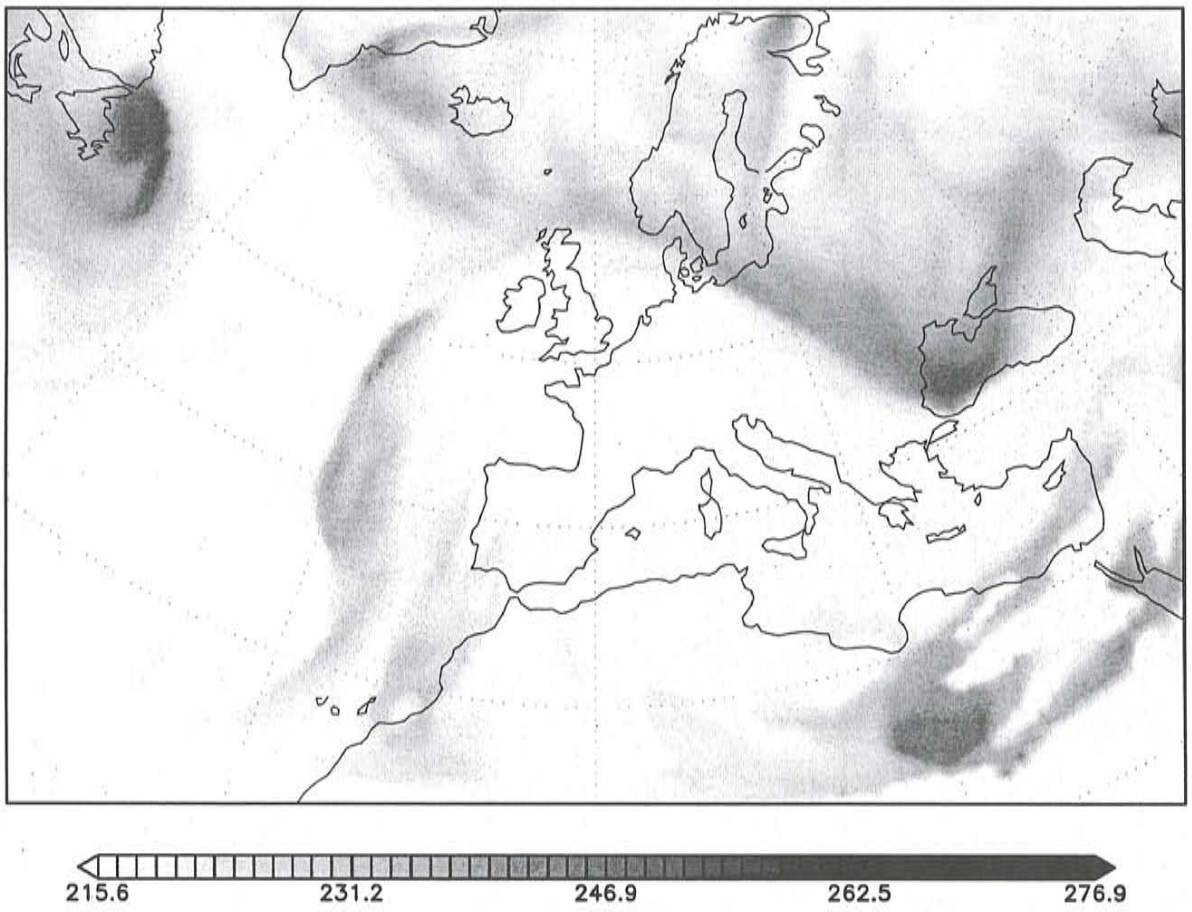

Figure 4.4: *The temperature (K) at the dynamic tropopause for the 29th of October 2002, 06 UTC.*

does represent transitions in the temperature at the tropopause. It seems that the humidity above the mentioned area is too high in the analysis, resulting in too much absorption and no sharp boundary in the synthetic water vapour image. If we would use a forecast instead of an analysis, large structures might be better represented in the synthetic images, because the longer the forecast period, the better the humidity adapts to the dry dynamic fields. In Section 4.2, we will investigate this expectation using the +24h forecast for the same time.

4.1.3 Comparison of (brightness) temperatures along 50N

To get a more quantitative view, Fig. 4.5 gives the brightness temperature values at the top of the atmosphere from Figs. 4.1 and 4.2 and the temperature values from Fig. 4.4 along the 50N latitude. The position of this latitude can best be seen in Fig. 4.4. There, the faint dotted lines represent latitudes every 10 degrees and longitudes every 20 degrees. The difference between the tropopause temperature and the brightness temperatures is very clear. The real water vapour image shows much more detail and often lower values, which are for a large part due to high clouds. But still, for the 50N latitude, the brightness temperature in

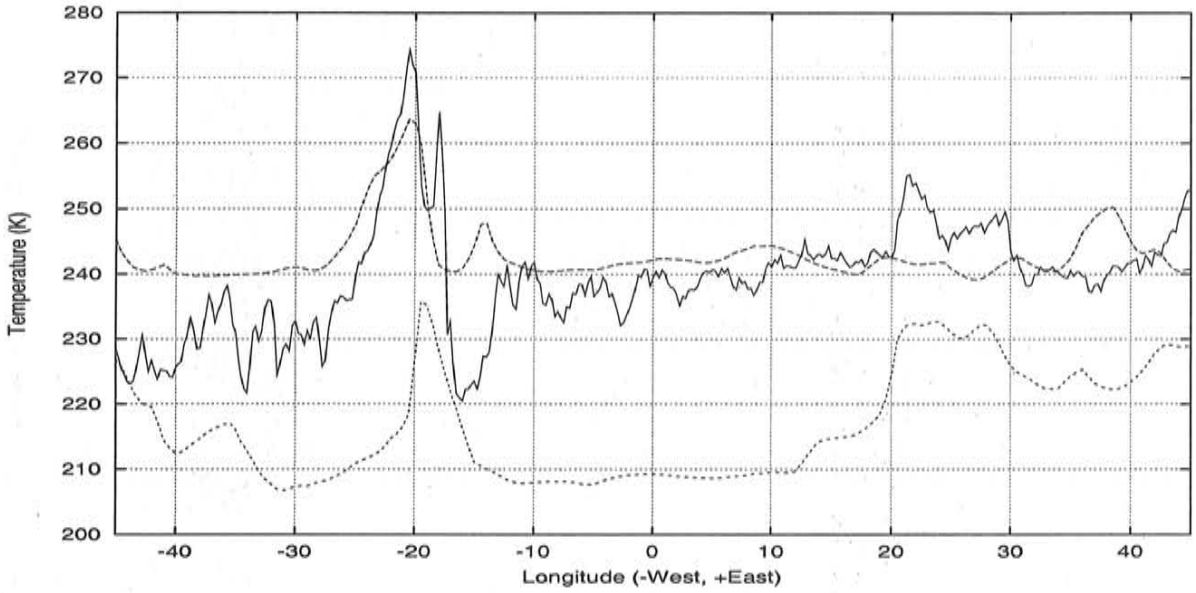

Figure 4.5: *The brightness temperature at the top of the atmosphere of the real water vapour (solid line), synthetic water vapour (long dashed line) and the temperature at the dynamic tropopause (short dashed line) along the 50N latitude.*

the synthetic image is of the same order as that of the real image. It is clear that the dark area at 20W is present in all lines. The tropopause temperature peak at 20W is situated a little more to the east. The real water vapour image shows two peaks around 20W, with in between a brighter value due to high cloudiness. If this cloudiness could be eliminated, it is likely that there is one peak that is also situated a bit more to the east, relative to the peak of the synthetic image. The dark area at 20E only shows up in the real water vapour image and the tropopause temperature image.

4.1.4 Cross-section of humidity and potential vorticity along 50N

To understand these features, in Fig. 4.6, we present a vertical cross-section of the potential vorticity and the specific humidity along 50N. Looking at the potential vorticity, we see that the tropopause (2 PVU surface) depression near 20W lies indeed a bit more to the east than the dark spots in the synthetic water vapour image. The humidity distribution near 20W is, as expected, in good agreement with the synthetic water vapour images. We see that between 25W and 20W there is only substantial water vapour in the lower atmosphere, resulting in a high brightness temperature. To the west of 25W, the specific humidity in the middle troposphere seems to be large enough for absorption of the upwelling radiation, making the brightness temperature much lower than between 25W and 20W. Although the humidity decrease somewhat going from 15E to 20E, the humidity distribution near 20E shows no sharp boundary as it does near 20W. Therefore, the synthetic water vapour image does not show a dark area near 20E. A possible explanation is that humidity is not represented well in the analysis, because this area has few observations. Also, the shift between the dark spot

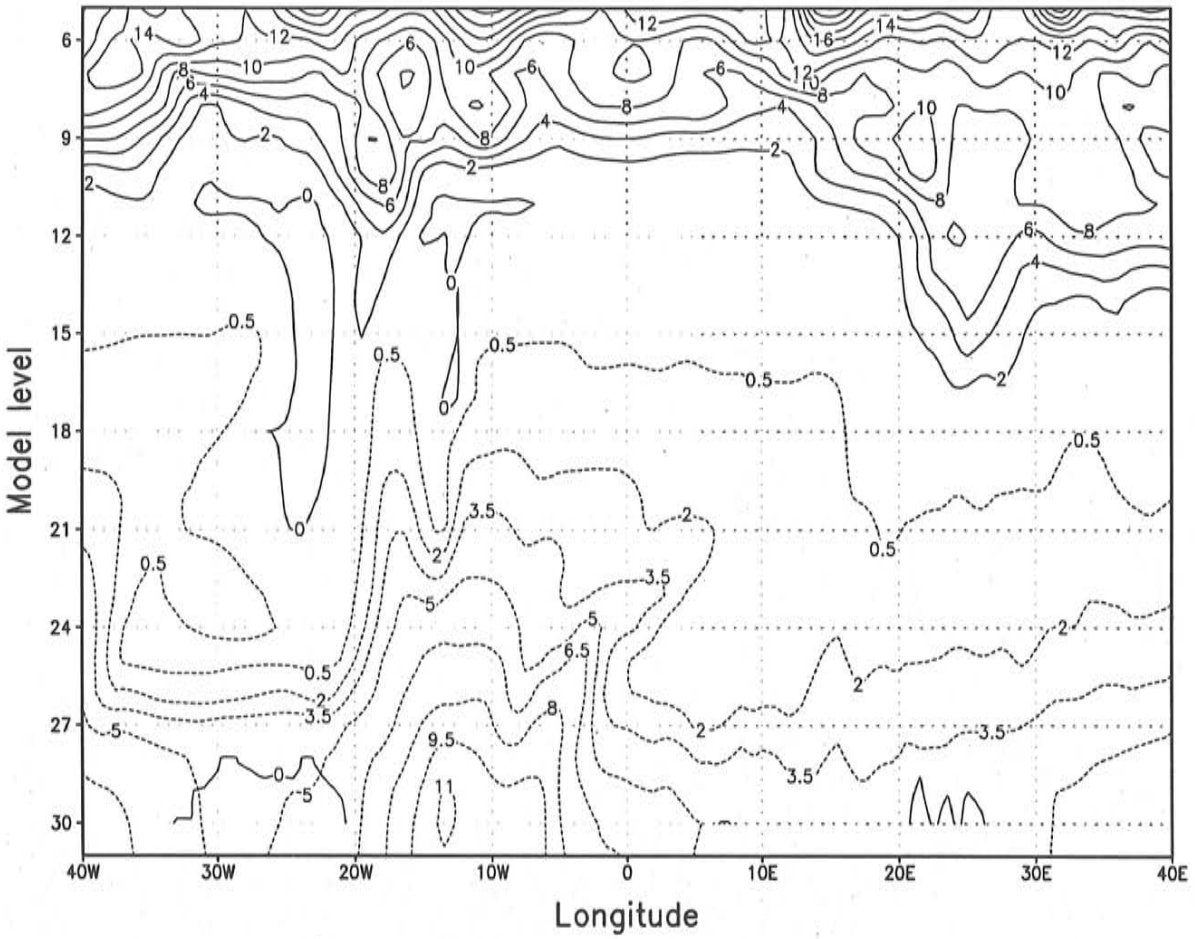

Figure 4.6: *Vertical cross-section along the 50N latitude of the potential vorticity in PVU (solid line) and the specific humidity in g/kg (dashed line). The pressure at the model levels depends on the surface pressure, but roughly the model levels may be regarded as pressure levels. Level 12 lies around 265 hPa, level 21 around 620 hPa.*

in the synthetic water vapour image and the potential vorticity anomaly, might disappear if we work with a forecast, because it is expected that the moisture will adapt to the dry dynamics. Therefore, in the next section, we will look at the +24h forecast for the same date and time.

4.2 Forecast for the 29th of October 2002 06 UTC

We will use the +24h forecast from the analysis of the 28th of October 2002 06 UTC, in order to investigate the expectations that the humidity will be better represented in forecasts. Firstly, we hope that the dark area over eastern Europe will show up and secondly, that the shift between the dark area in the synthetic water vapour images and the potential vorticity anomaly near 20E will diminish.

4.2.1 Synthetic water vapour image

In Fig. 4.7, the synthetic water vapour image is presented. In comparison with the analysis

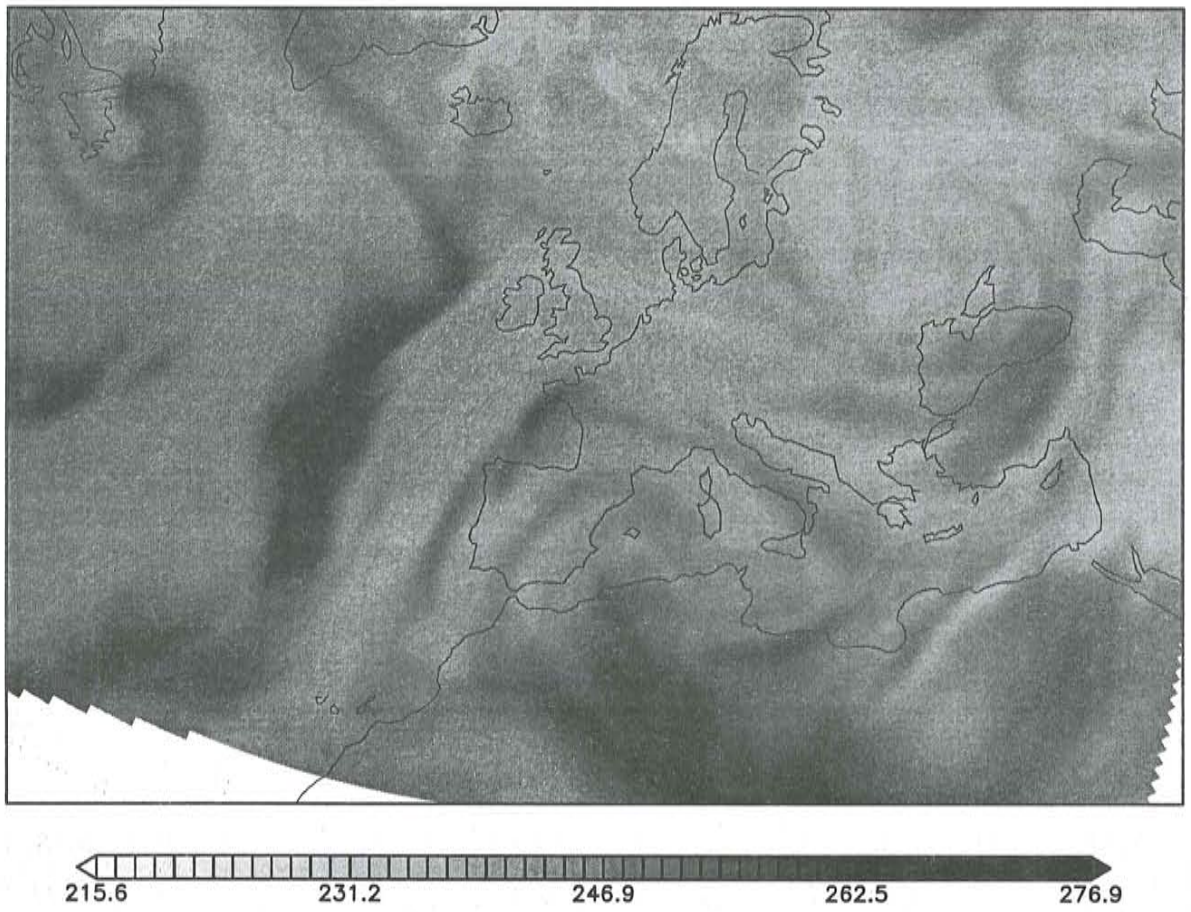

Figure 4.7: *Synthetic water vapour image for the +24h forecast, valid for the 29th of October 2002, 06 UTC (brightness temperature in Kelvin).*

in Fig. 4.2a, the forecast synthentic water vapour image indeed shows a darker area over eastern Europe, but it is not very distinctive. We also see that the dark spot near 20W has a different shape, but there does not seem to be a shift in the location. The northern boundary of the bright band that lies over the north of Great Britain, is located more to the north.

4.2.2 Temperature at the dynamic tropopause

The temperature at the dynamic tropopause is given in Fig. 4.8. Here too, the northern boundary mentioned in the previous section, lies more to the north. The higher temperature area near 20W shows another shape than the area in Fig. 4.4.

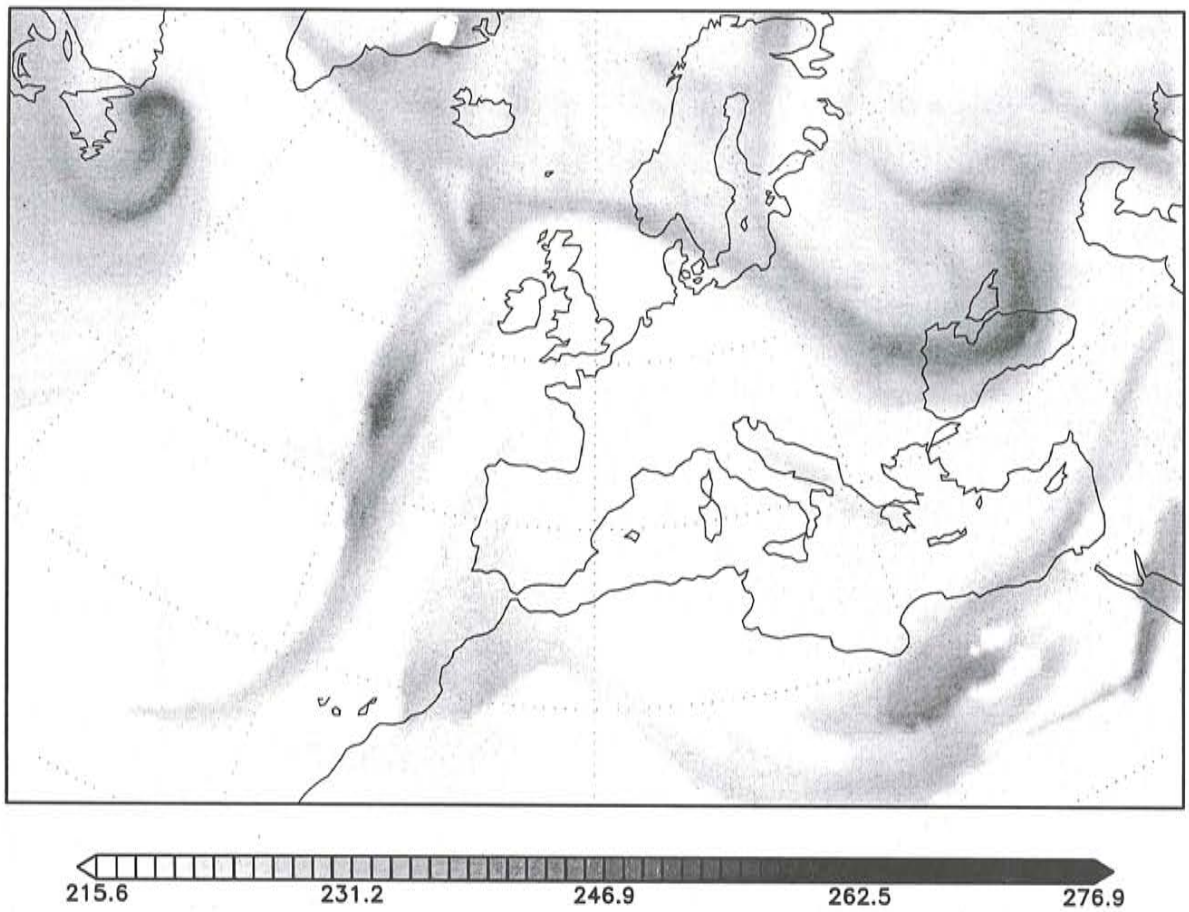

Figure 4.8: *The temperature (K) at the dynamic tropopause for the +24h forecast, valid for the 29th of October 2002, 06 UTC.*

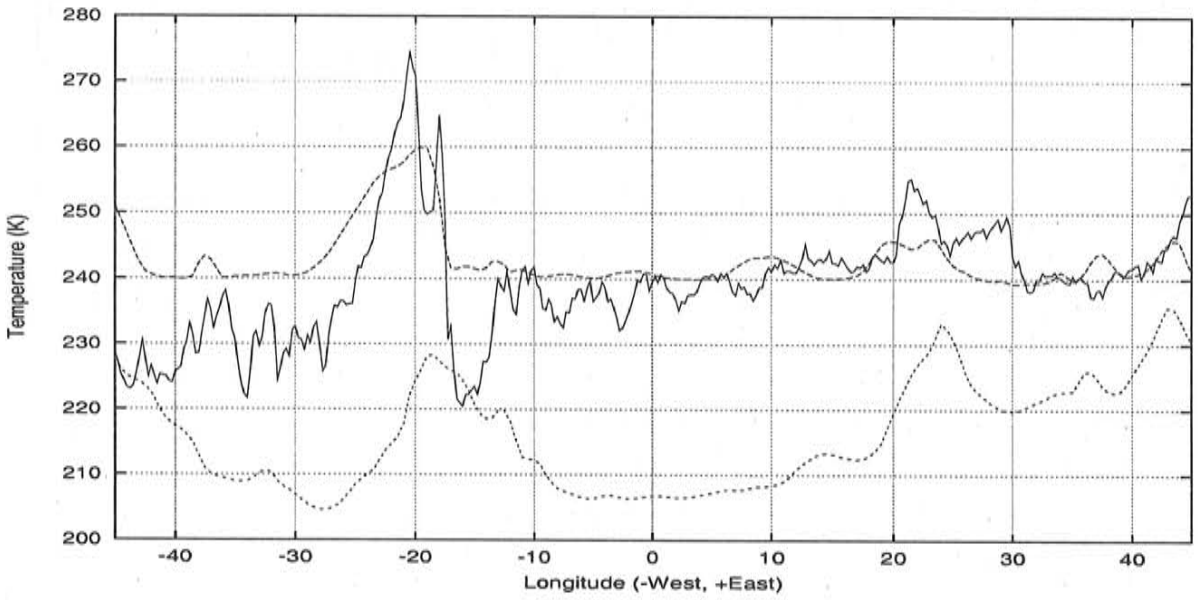

Figure 4.9: *The brightness temperature at the top of the atmosphere of the real water vapour (solid line), the synthetic water vapour (long dashed line) and the temperature at the dynamic tropopause (dotted line) along the 50N latitude, for the +24h forecast.*

4.2.3 Comparison of (brightness) temperatures along 50N

Again, we will take a look at the (brightness) temperature values at the top of the atmosphere from Figs. 4.7 and 4.8 along the 50N latitude (Fig. 4.9). This can directly be compared to Fig. 4.5.

The dark area near 20E is more pronounced in the synthetic water vapour image from the forecast in comparison with the image from the analysis. Looking at 20W, the peaks of the brightness temperature from the synthetic image and the temperature at the tropopause are located at the same longitude. However, the steep side of the peak in the synthetic water vapour image lies to the east of the peak, whereas the tropopause temperature shows a steep side to the west. This still implies a shift between the dark area in the synthetic water vapour images and the potential vorticity anomaly near 20W.

4.2.4 Cross-section of humidity and potential vorticity along 50N

The still existing shift near 20W can also be seen in Fig. 4.10. In comparison with the

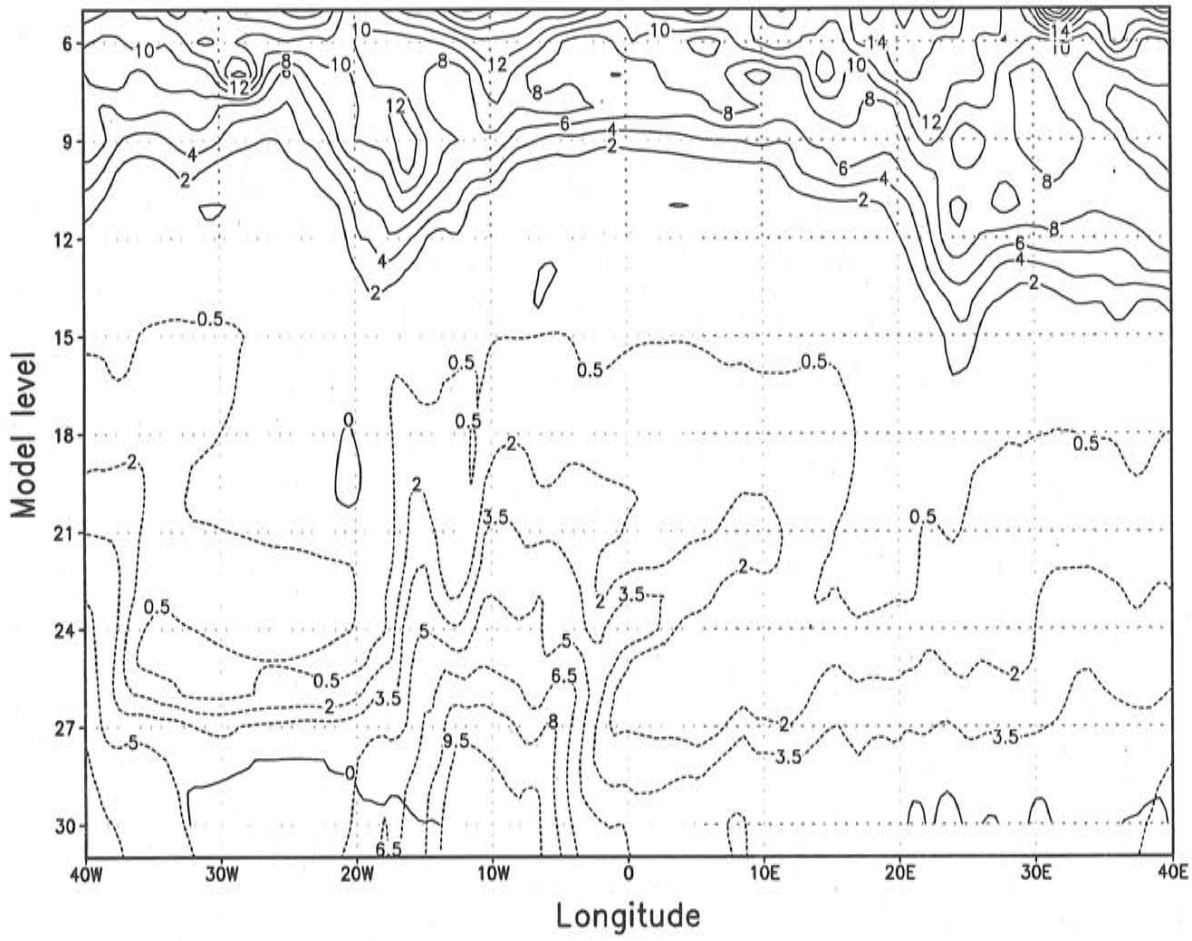

Figure 4.10: *Vertical cross-section along the 50N latitude of the potential vorticity in PVU (solid line) and the specific humidity in g/kg (dashed line), for the +24h forecast.*

analysis, Fig. 4.6, the peak in the potential vorticity seems to lie a little bit more above the dry region near 20W, that has itself moved somewhat eastwards. The potential vorticity anomaly extends over a larger area, making the dark area in Fig. 4.8 wider. The dark area in the synthetic water vapour image has widened too, but it has extended more westward. This is the result of the westwards shift of the humidity between levels 15 and 18, near 30W. We see that the humidity to the west of 20E is lower in the forecast, making the dark area over eastern Europe more visible. The different shape of the peak in the tropopause temperature near 20E, is explained by the narrowing of the potential vorticity anomaly.

4.3 Potential vorticity overlay

Having compared (brightness) temperatures, humidity and potential vorticity along a latitude, we will now extend our view to full images. Fig. 4.11 shows the overlay of the model potential vorticity at the 318 K isentropic surface over the synthetic water vapour image, for both the analysis and the +24h forecast. Regarding, the position of the potential vorticity boundaries in relation to the dark areas in the water vapour images, there does not seem to be a substantial difference between the analysis and forecast. These figures clearly show that only the system that is located near 20W shows a shift between the potential vorticity and the water vapour image. The position of the deep low over New-Foundland, Canada, in the water vapour image is in agreement with the potential vorticity field. This is also true for the potential vorticity boundary over eastern Europe, which lies parallel to the streamlines near the polar jet stream. The system near 20W is a kind of isolated trough, that has developed into a surface low. The potential vorticity anomaly stretches out perpendicular to the west-east flow higher in the troposphere. This is where the explanation of the shift between the potential vorticity field and the synthetic water vapour image may lie. Perhaps, near these kind of systems, the humidity is badly represented in both the analysis and forecast. In order to confirm this statement, it is necessary to investigate more cases similar to the one we studied.

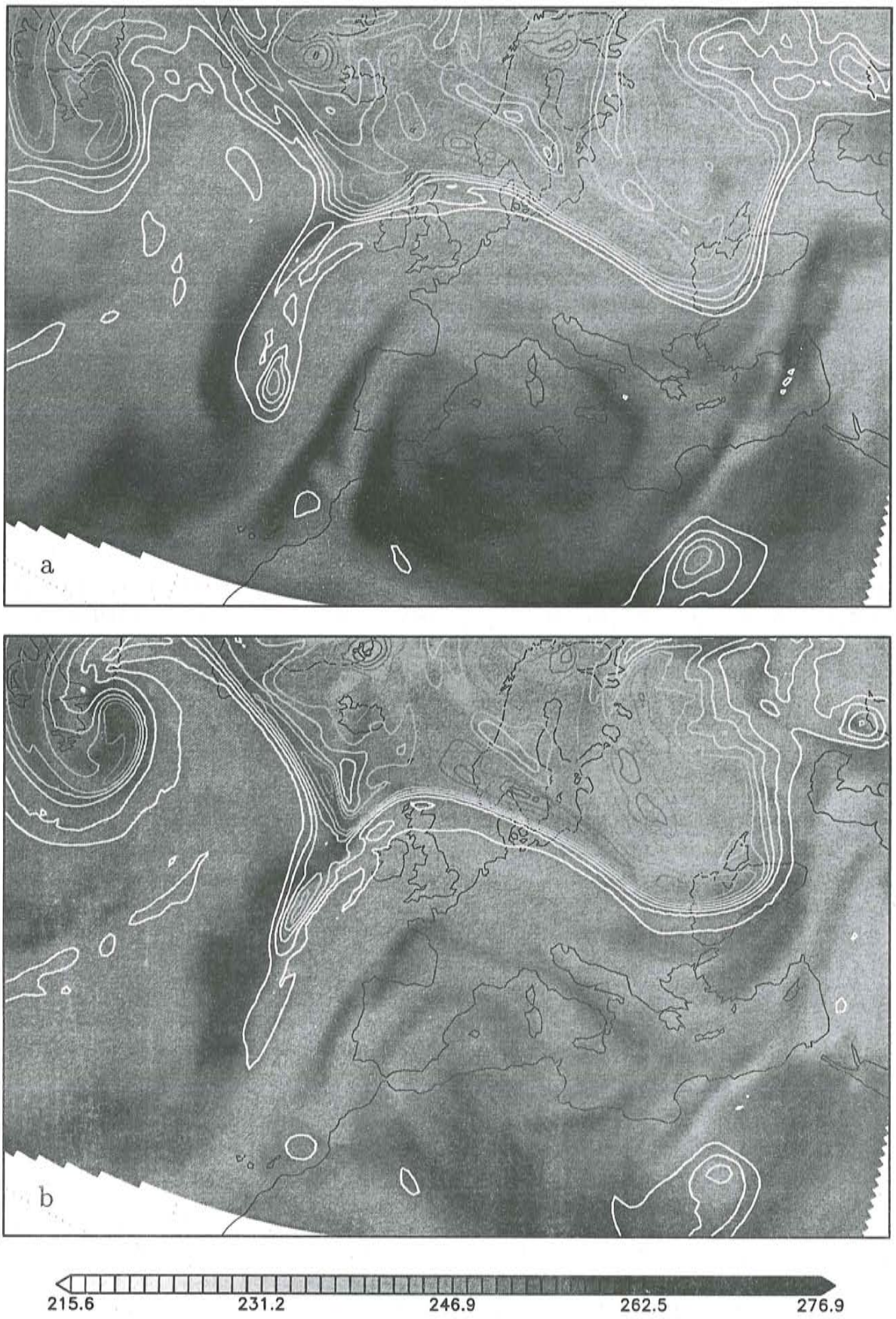

Figure 4.11: *Synthetic water vapour image (K) and potential vorticity (PVU) at the 318 K isentropic surface for a) the analysis and b) the +24h forecast. Potential vorticity is plotted every 1 PVU, from 1 PVU (white) up to 12 PVU (dark grey).*

Chapter 5

Improving Tijm's method

5.1 Implementing the pressure and temperature dependence of the absorption in Tijm's method

As we have seen in Section 3.2.3.2, Tijm's method seems to overestimate the absorption in the upper troposphere. Our radiative transfer model, on the other hand, works with an absorption coefficient that depends on pressure and temperature. As a result, a layer in the upper troposphere that contains as much water vapour as a layer in the lower troposphere, does not absorb as much radiation. In Tijm's method, the amount of absorption is determined by the treshold value q_{wv}, which does not vary throughout the atmosphere. Therefore, we will improve the method by implementing a pressure and temperature dependence of q_{wv}.

This dependence is given in Eq. (3.17) by:

$$\left(\frac{p}{p_0}\right)^n \left(\frac{T_0}{T}\right)^m,$$

where n=0.9834 and m=-2.5294. This will reduce the absorption coefficient for lower pressure and temperature values. If we want the same effect in the Tijm model, q_{wv} needs to increase with decreasing pressure and temperature. Therefore, in a first attempt to improve the model, we will multiply q_{wv} with the inverse of the above mentioned dependence:

$$\left(\frac{p_0}{p}\right)^n \left(\frac{T}{T_0}\right)^m.$$

Eq. (3.1) then becomes:

$$T_B = T_{B,old}\left(1 - MIN\left[1, \left(\frac{q\Delta p}{q^*_{wv}}\right)\right]\right) + T_a\left(MIN\left[1, \left(\frac{q\Delta p}{q^*_{wv}}\right)\right]\right), \tag{5.1}$$

$$with \quad q^*_{wv} = q_{wv}\left(\frac{p_0}{p}\right)^n \left(\frac{T}{T_0}\right)^m$$

If we do not change the value of q_{wv} (3.0 Pa), this results in an overestimation of the absorption. So, we need to decrease the value of q_{wv}. We can do this experimentally by

taking the value that fits best for several profiles. We did not only use the profiles of the four points in Chapter 3, but we also looked at the values of the 50N latitude from the analysis in Chapter 4. This leads to a value of 0.85 Pa.

To illustrate the improvement, we will first present the brightness temperature profiles for two single gridpoints. These are points 3 and 4 from Chapter 3, which serve as examples of respectively a gridpoint for which Tijm's original method gives more or less the same output at the top of the atmosphere (3), and of a gridpoint for which Tijm's original method gives a brightness temperature that is too low (4). Fig. 5.1 shows the same profiles as Fig. 3.6, plus the profile for Tijm's adapted method. It is clear that in the lower troposphere, the

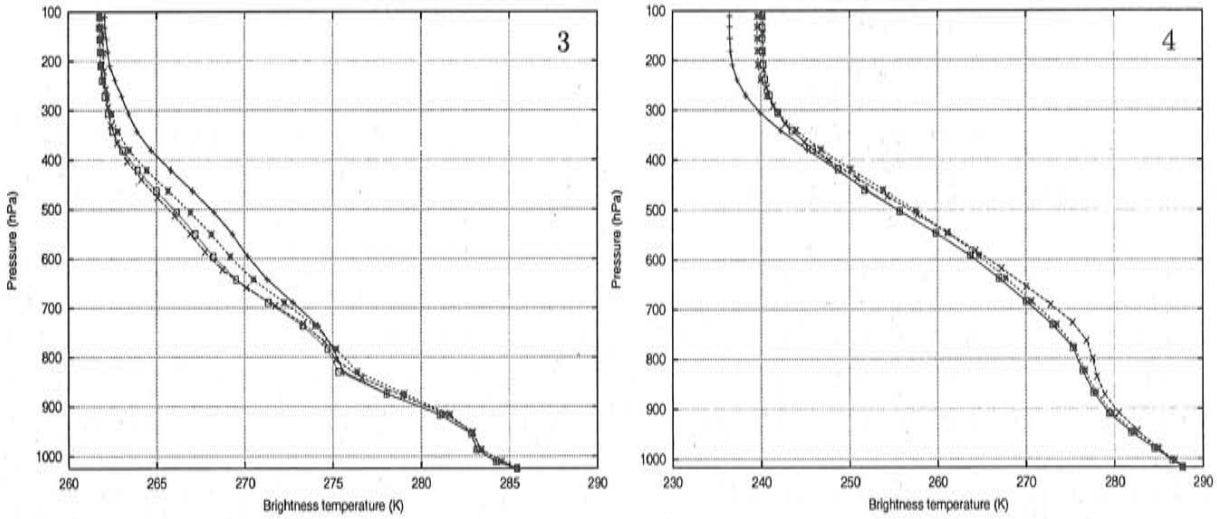

Figure 5.1: *Brightness temperature profiles by the original Tijm model(+), the radiative transfer model (X), the reference model Modtran4(*) and the adapted Tijm model (□) for points 3 and 4.*

adapted Tijm profile is equal to the original Tijm profile, and higher up in the troposphere it adapts to the profile based on radiative transfer. If we compare it to the reference Modtran4 profile, over a large part of the atmosphere, the profile of point 3 has just shifted to the other side of the Modtran4 profile and still shows no agreement. However, we are interested in the value at the top of the atmosphere. Tijm's adapted method shows better agreement with both Modtran4 and the radiative transfer model, than Tijm's original method. The value for point 4 has adapted well, whereas the value for point 3 has not changed much.

If we extend our view to the synthetic water vapour images, it becomes clear that indeed Tijm's adapted method resembles the radiative transfer model remarkably well. Fig. 5.2 shows the synthetic water vapour image for the analysis of the 29th of October 2002, 06 UTC calculated by Tijm's adapted method. Comparing it with Fig. 4.2, the synthetic image calculated by the radiative transfer model, the resemblance is obvious. Fig. 5.3a shows the brightness temperature values at the top of the atmosphere along the 50N latitude, for the analysis of the 29th of October 2002 06 UTC. As a reference, the values of Tijm's original method are presented too. As is clear from the figure, the output of Tijm's adapted method is in very good agreement with the output from the radiative transfer model. In

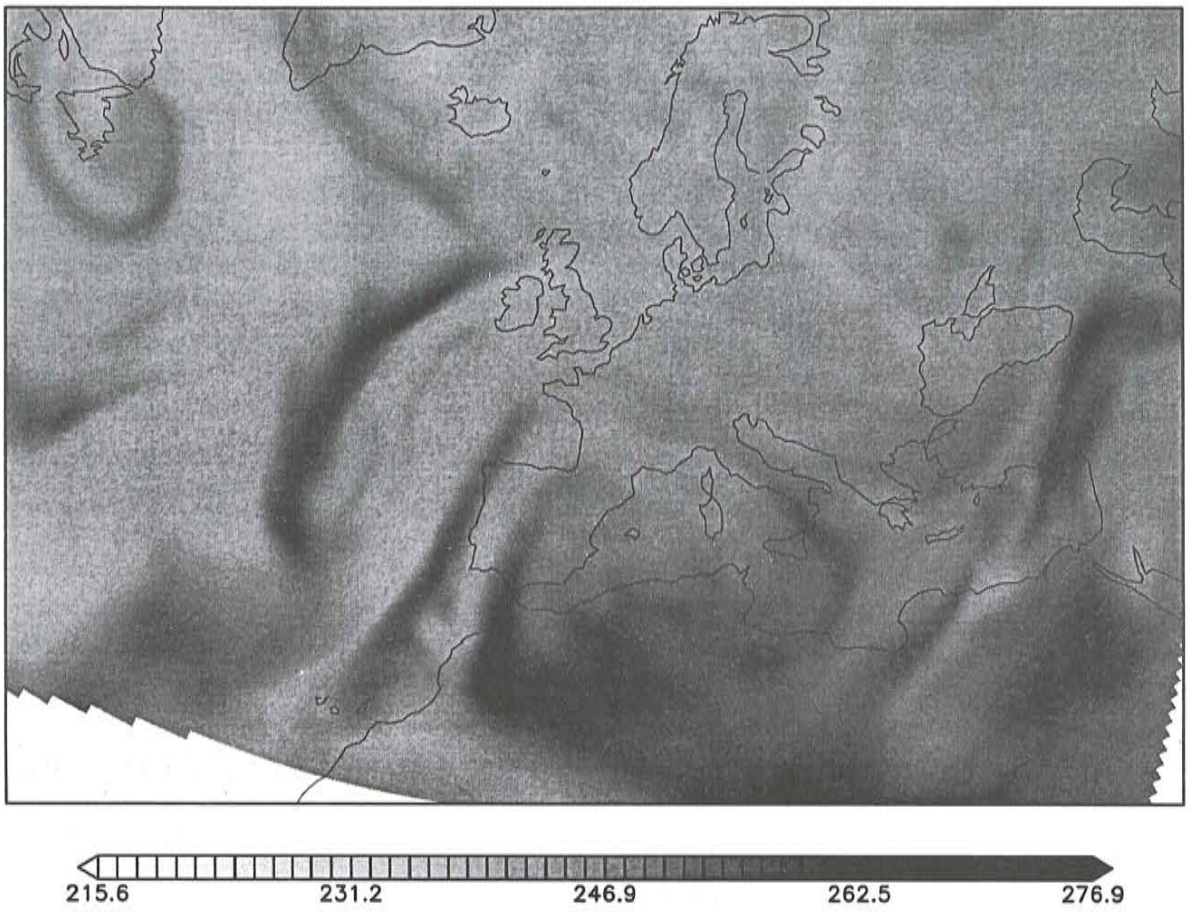

Figure 5.2: *The synthetic water vapour image calculated by Tijm's adapted method for the analysis of the 29th of October 2002, 06 UTC (brightness temperature in Kelvin).*

Fig. 5.3b, the differences between the radiative transfer model and both Tijm's adapted and original method are shown. The adapted method lies near zero, except near 25W and 15W. However, the difference there is still small in comparison with the difference between the radiative transfer model and Tijm's original method.

The output of the adapted method is in such a good agreement with the output of the radiative transfer model, that this can hardly be a coincidence. Although at first sight, the methods really differ in their calculations of the brightness temperature at the top of the atmosphere, we will show that Tijm's method can be derived from the equations of radiative transfer. For that purpose, we need to write the equations of both methods in a differential form.

5.2 Differential equation for Tijm's method

We will write Eq. (5.1) in terms of the change in brightness temperature between two atmospheric levels. We distinguish two cases. In the first, there is full absorption ($q\Delta p > q^*_{wv}$) and the brightness temperature takes over the value of the air temperature. In the second case,

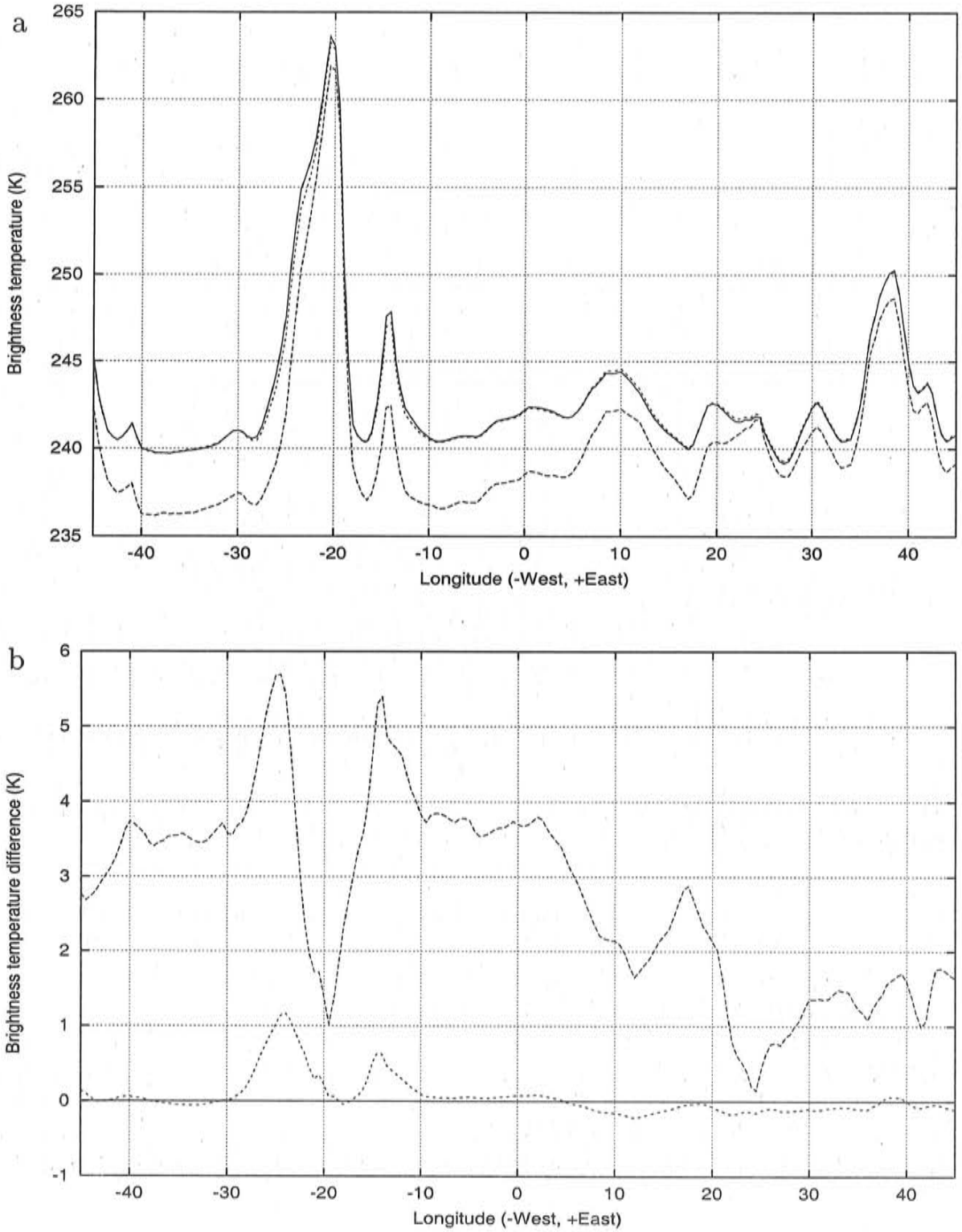

Figure 5.3: *Values along the 50N latitude of a) the brightness temperature at the top of the atmosphere of the radiative transfer model (solid line), Tijm's original method (long dashed line) and Tijm's adapted method (short dashed line) and b) the difference in brightness temperature between the radiative transfer model and Tijm's original method (long dashed line) and Tijm's adapted method (short dashed line).*

there is no full absorption ($q\Delta p < q^*_{wv}$) and the adaption of the brightness temperature is only a fraction of the difference between the air temperature and the brightness temperature at the previous level. So, Tijm's method can be written in terms of the following equations:

$$\begin{aligned} &if \quad \frac{q(-\Delta p)}{q^*_{wv}} > 1 \quad then \quad \Delta T_B = (T_a - T_B) \\ &if \quad \frac{q(-\Delta p)}{q^*_{wv}} < 1 \quad then \quad \Delta T_B = (T_a - T_B)\frac{q(-\Delta p)}{q^*_{wv}}. \end{aligned} \tag{5.2}$$

Since the radiation travels towards lower pressure values, we introduced a minus before Δp, in order to have a positive pressure interval. This formal subtlety will be needed in the comparison of the differential equations of Tijm's method with the differential equation of radiative transfer.

5.3 Differential equation for radiative transfer

Our radiative transfer model is based on the formal solution of the Schwarzschild equation, Eq. (3.12). As we have mentioned in Section 3.2.1, the Schwarzschild equation could also be integrated directly. In order to look upon Tijm's method from this perspective, we express $I_\nu(p)$ and $B_\nu(p)$ in terms of temperature. B_ν is the black body radiance belonging to the radiation emitted by water vapour in the atmosphere. This radiation is emitted at the air temperature (T_a). Referring to Eq. (3.16), the spectral radiance I_ν is the black body radiance corresponding to the brightness temperature. So we write:

$$I_\nu(p) = B_\nu(T_B) \tag{5.3}$$

$$B_\nu(p) = B_\nu(T_a). \tag{5.4}$$

Since values for T_B and T_a are of the same order, we may linearize this as follows:

$$I_\nu(p) \cong B_\nu(T_0) + (T_B - T_0)\left(\frac{dB_\nu}{dT}\right)_{T_0} \tag{5.5}$$

$$B_\nu(p) \cong B_\nu(T_0) + (T_a - T_0)\left(\frac{dB_\nu}{dT}\right)_{T_0}, \tag{5.6}$$

where $B_\nu(T_0)$ and $\left(\frac{dB_\nu}{dT}\right)_{T_0}$) are constants. If we substitute this in Eq. (3.11), we get:

$$dT_B\left(\frac{dB_\nu}{dT}\right)_{T_0} = (T_B - T_a)\left(\frac{dB_\nu}{dT}\right)_{T_0} k_\nu q\frac{dp}{g}. \tag{5.7}$$

Dividing this by the constant $\left(\frac{dB_\nu}{dT}\right)_{T_0}$, we obtain:

$$dT_B = (T_a - T_B)q(-dp)\frac{k_\nu}{g}. \tag{5.8}$$

Eq. (5.8) can be integrated directly and using an advanced integration method, like a fourth-order Runge-Kutta method (Section 15.1 in [11]), we may construct brightness temperature profiles and subsequently synthetic water vapour images. Working with N intervals, the number of operations in a computer code would be proportional to N; in our method based on the formal solution, this number is proportional to N^2, because both the radiance and the optical depth have to be integrated using N intervals. So, the direct method requires less computation time.

5.4 Tijm's method related to radiative transfer

If we look closely at Eqs. (5.2) and (5.8), it is obvious that Tijm's equation in the case that there is no full absorption, has the same form as the radiative equation. So, we have found the link between Tijm's method and radiative transfer. In Section 5.1 we found by experiment that q_{wv} should have the value 0.85 Pa. Now, we can also deduce its value from Eqs. (5.2) and (5.8). We find that

$$q^*_{wv} = \frac{g}{k_\nu}, \tag{5.9}$$

which can be fully written as:

$$q_{wv}\left(\frac{p_0}{p}\right)^n\left(\frac{T}{T_0}\right)^m = \frac{g}{C'}\left(\frac{p_0}{p}\right)^n\left(\frac{T}{T_0}\right)^m. \tag{5.10}$$

This leads to the following value for q_{wv}:

$$q_{wv} = \frac{g}{C'} = \frac{9.80616}{14.0} = 0.70\ Pa, \tag{5.11}$$

which is of the same order as the value 0.85 Pa, which we found experimentally. The difference may lie in the fact that Tijm's method works with the brightness temperature, whereas the radiative transfer model works with radiance and only at the end converts the radiance into the brightness temperature. Since their relation is not linear (see Fig. 3.3), the experimentally determined value and the derived value may differ. However, in a first quick experiment where the brightness and air temperature in Tijm's equation are replaced by the corresponding radiances, the value of 0.70 Pa does not show a better result. In order to look at this more closely, more investigation is needed.

In case of full absorption, we could probably also work with Tijm's equation for partly absorption if we take pressure intervals that are small enough. We have seen this in our radiative transfer model too. In the lower atmosphere, we need to work with more and smaller pressure intervals, which takes more computation time, in order to get a reliable profile. In the lower troposphere, the profile lies close to the air temperature profile, because enough water vapour is present for full absorption. The first equation in Tijm's method, as expressed by Eq. (5.2), is now seen to be a clever shortcut of a calculation that would otherwise take much more time. It just states immediately that if the water vapour content exceeds a certain treshold value, de brightness temperature takes over the value of the air temperature.

Concluding, we can make some recommendations for the use of Tijm's method. Firstly, we advise to use q^*_{wv}, the treshold value that is corrected for the pressure and temperature dependence of absorption. Furthermore, it would be worthwhile to work with radiance instead of brightness temperature, because the process of the absorption of upwelling radiation is described by the intensity of the radiation. Once the radiance at the top of the atmosphere is known, it can be converted into the brightness temperature. Finally, it is of interest to investigate more precisely when Tijm's shortcut of full absorption is justified.

For the construction of water vapour images, Tijm's method is superior to our method, because it requires considerable less computation time. However, the disadvantage of Tijm's method is that it does not give as much insight as our method. Our method is suitable for the investigation of the origin of the radiation that reaches any level in the atmosphere.

Chapter 6

Conclusions and Recommendations

We have developed a simple radiative transfer model for the upwelling radiation in the water vapour absorption band (5.7-7.1μm), in which we account for the absorption of radiation by water vapour in the atmosphere. The advantage of the model, which is based on the formal solution of the Schwarzschild equation for radiative transfer, is that one is able to understand the radiance contribution throughout the atmosphere. Using this model, we have constructed brightness temperature profiles for single gridpoints and synthetic water vapour images for a field of gridpoints.

We have seen that the vertical distribution of water vapour throughout the atmosphere is very important in determining the brightness temperature at the top of the atmosphere. Not only does it determine which part of the atmosphere contributes to the upwelling radiation that reaches the top of the atmosphere, but it also has great influence on the magnitude of the contribution.

In general, the synthetic water vapour images resemble real water vapour images. However, not all structures of a real image, can be reconstructed by the radiative transfer model. We do not understand why real water vapour images show darker grey shades (higher brightness temperatures) in the south. The HIRLAM model does not seem to badly represent humidity and temperature in this region and neither can it be explained by the fact that we do not work with slant radiation paths. In order to get more insight into this, more research is needed.

We have also seen that in certain areas a HIRLAM analysis may not represent sharp transitions in humidity very well, resulting in the absence of some boundaries in the synthetic image. Since humidity tends to adapt to the dry dynamics in a model run, we have looked at the +24h forecast too. The forecast shows some improvements over eastern Europe, but it does not result in the adaption needed to resemble the real water vapour image. We did not investigate the issue of humidity representation in areas with few observations any further. We suggest this as a topic for further research.

We have shown that the assumption that the troposphere contains enough water vapour to fully absorb the upwelling radiation and that the stratosphere is completely dry, is quite inaccurate. Of course, the stratosphere does not contain substantial water vapour. However, the humidity distribution in the troposphere is not given by a 100% relative humidity profile. But even if this would be the case, there would still not be enough water vapour in the upper

troposphere to fully absorb the upwelling radiation from beneath. Therefore, it is clear that a water vapour image does not reflect the height of the tropopause. However, we proved that it is still useful to compare the temperature at the dynamic tropopause with water vapour images. Sharp transitions of large structures are in good agreement.

Regarding the relationship between potential vorticity and water vapour imagery, we have only succeeded in qualifying it. The mismatch between the potential vorticity anomaly and the dark area in the isolated trough near 20W, is still not understood. We hoped that using a forecast would make the mismatch disappear. However, the humidity does not show an adaption to the dry dynamics like the temperature at the dynamic tropopause. It seems worthwhile to look at more cases with similar dynamic structures in order to understand these kind of mismatches. We have shown that the water vapour image is not fully determined by dry dynamics, like the height of the tropopause, and it is therefore at this moment not possible to quantify the relationship. It seems a real challenge for further research.

After implementing the pressure and temperature dependence of the absorption in Tijm's method, its output remarkably resembles the output of the radiative transfer model. We have shown that indeed there is a relation between the two methods. Although Tijm did not develop his method on the basis of radiative transfer theory, it can be derived from the equations for radiative transfer, if we use the differential form of both the Schwarzschild equation and the equation on which Tijm's method is based.

The direct integration of the differential form requires less computation time than the integration of the formal solution of the Schwarzschild equation. Working with N intervals, the number of operations in the computer code of the direct integration is proportional to N; in our method based on the formal solution, this number is proportional to N^2, because both the radiance and the optical depth have to be integrated using N intervals. Tijm's method is even faster, because of the shortcut it makes in the lower atmosphere. So, for the construction of water vapour images, we prefer Tijm's method. However, both Tijm's method as well as the direct integration of the Schwarzschild equation, does not give information of the radiance contribution throughout the atmosphere. For that purpose, the formal solution must be used.

For practical reasons, we did not include the absorption by clouds. For a better understanding of the meaning of water vapour imagery, this can no longer be neglected. So, we recommend investigation of the absorption by clouds and implementing this process into the radiative transfer model. The absorption is determined by the amount of absorbing substance (like the water vapour content) and the efficiency with which the absorption occurs (the spectral absorption coefficient). In order to include clouds, the cloud water content, that is also a prognostic variable in the HIRLAM model, is to be used. The spectral absorption coefficient depends on the absorbing substance. So, next to the value for C' (Eq. 3.17) we use for water vapour, another value must be used for clouds. Of course, clouds should be accounted for in Tijm's method too, whether in an intuitive way or based on radiative transfer.

Since we know now that Tijm's method is related to radiative transfer, we can make some recommendations for the improvement of the method. Firstly, we advise to use q^*_{wv}, the treshold value that is corrected for the pressure and temperature dependence of absorption. Furthermore, it would be worthwhile to work with radiance instead of brightness

temperature, because the process of the absorption of upwelling radiation is described by the intensity of the radiation. Once the radiance at the top of the atmosphere is known, it can be converted into a brightness temperature. Finally, it is of interest to investigate more precisely when Tijm's shortcut of full absorption is justified.

Since we are not sure about the right representation of humidity by the HIRLAM model in areas with few observations and near isolated troughs, it would be of interest to use input from other numerical weather prediction models, like the ECMWF model, to further study this aspect of the problem.

In this study, we compare the synthetic water vapour images with a real water vapour image from the first generation of Meteosat. Recently, Meteosat Second Generation (MSG) has been launched and images are expected to become available soon. It has two channels in the water vapour absorption band, one centered around 6.2 μm and the other around 7.3 μm. The contribution functions of these channels have their maximums at different heights in the troposphere. As a result, MSG will supply more information of the humidity distribution throughout the troposphere. In this light, it is worthwhile to adapt our radiative transfer model to each of the channels. Since the water vapour channels of MSG give information of the humidity at different heights, MSG is likely to give more insight into the relationship between potential vorticity and water vapour imagery.

Bibliography

[1] Bader, M.J., G.S. Forbes, J.R. Grant, R.B.E. Lilley and A.J. Waters, 1995: Images in weather forecasting. A practical guide for interpreting satellite and radar imagery. Cambridge University Press.

[2] Berk, A., G.P. Anderson, P. Acharya, J.H. Chetwynd, L.S. Bernstein, M.W. Matthew and S.M. Adler-Golden, 1999: Modtran4 User's Manual. *Air Force Research Laboratory, Space Vehicles Directorate, Air Force Material Command, Hanscom AFB.*

[3] Curry, J.A. and P.J. Webster, 1999: Thermodynamics of atmospheres and oceans. Academic Press.

[4] Demirtas, M. and A.J. Thorpe, 1998: Sensitivity of short-range weather forecasts to local potential vorticity modifications. *Mon. Wea. Rev.*, **127**, 922-939.

[5] Holton, J.R.,1992: An introduction to dynamic meteorology, third edition. Academic Press.

[6] Hoskins, B.J., M.E. McIntyre and A.W. Robertson, 1985: On the use and significance of isentropic potential vorticity maps. *Quart. J. Roy. Meteor. Soc.*, **111**, 877-946.

[7] Källén, E. (editor), 1996: HIRLAM documentation manual, system 2.5. Manual, The international HIRLAM project.

[8] Kneizys, F.X., L.W. Abreu, G.P. Anderson, J.H. Chetwynd, E.P. Shettle, A. Berk, L.S. Bernstein, D.C. Robertson, P. Acharya, L.S. Rothman, J.E.A. Selby, W.O. Gallery and S.A. Clough, 1996: The MODTRAN 2/3 Report and LOWTRAN 7 MODEL. *MODTRAN Report 1/11/96, Philips Laboratory, Geophysics Directorate, Hanscom AFB.*

[9] Liou, K.N., 2002: An introduction to atmospheric radiation. Second edition. Academic Press.

[10] Mansfield, D.A., 1996: The use of potential vorticity as an operational forecast tool. *Meteorol. Appl.*, **3**, 195-210.

[11] Press, W., Flannery, B.P., Teukolsky, S.A. and Vetterling, W.T., 1986: Numerical recipes. The art of scientific computing. Cambridge University Press.

[12] Reenen, M. van, 1999: Long-wave radiative transfer and water vapour satellite imagery. *Eindhoven University of Technology, Faculty of Physics, Report R-1478-A.*

[13] Roberts, N.M., 2000: A guide to aspects of water vapour imagery interpretation: the significance of dry regions. *Joint Centre for Mesoscale Meteorology (JCMM) Internal Report No. 109.*

[14] SatRep Manual, version 4.0, 02-04-2003
http://www.zamg.ac.at/docu/satmanu4.0/satmanu/main.htm.

[15] Tijm, A.B.C., 2002: Satellietbeelden gegenereerd met Hirlam. *Meteorologica*, **1**, 25-27.

[16] Vosbeek, P.W.C., W.T.M. Verkley and A.R. Moene, 2001: Manually adjusting a numerical weather analysis in terms of potential vorticity using three-dimensional variational data-assimilation. *Technical Report, BCRS, USP-2, No. 01-01.*

[17] Weldon, R.B. and S.J. Holmes, 1991: Water vapor imagery. Interpretation and applications to weather analysis and forecasting. *NOAA Technical Report NESDIS 57* .

[18] Wernli, H., S. Dirren, M.A. Liniger and M. Zillig, 2002: Dynamical aspects of the life cycle of the winter storm 'Lothar' (24-26 December 1999). *Quart. J. Roy. Meteor. Soc.*, **128**, 405-429.

Appendix A

Conversion of relative to specific humidity

This appendix follows for the most part Van Reenen's Appendix C.2 [12]. However, some values are based on other literature ([3]). The relative humidity, r, is the ratio between the actual specific humidity and the saturation specific humidity:

$$r = \frac{q}{q_s}. \tag{A.1}$$

So, for the conversion of relative into specific humidity, we need an expression for the saturation specific humidity. We deduce this from the *Clausius Clapeyron equation* in the liquid-vapour phase equilibrium of water, which is [3]:

$$\frac{de_s}{dT} = \frac{L_{lv}e_s}{R_v T^2}. \tag{A.2}$$

e_s is the water vapour saturation pressure, L_{lv} is the latent heat of vapourization (or condensation) and R_v is the gas constant of water vapour, 461.51 $\mathrm{Jkg^{-1}K^{-1}}$.

The rate of change of the latent heat of vapourization with temperature is equal to the difference between the specific heat capacity at constant pressure of the vapour (c_{pv}) and the specific heat capacity of the liquid (c_{pl}) [3]:

$$\frac{dL_{lv}}{dT} = c_{pv} - c_{pl}, \tag{A.3}$$

where c_{pv} and c_{pl} are respectively 1870 and 4218 $\mathrm{Jkg^{-1}K^{-1}}$ [3]. Neglecting the small variation in specific heat with temperature, integrating Eq. (A.3) yields:

$$L_{lv} = (c_{pv} - c_{pl})T + C_1, \tag{A.4}$$

where C_1 is an integration constant, that can be obtained by evaluating Eq. (A.4) at T=273.15 K, where L_{lv} is 2.501*10^6 $\mathrm{Jkg^{-1}}$ [3]. This gives C_1=3.142356*10^6 $\mathrm{Jkg^{-1}}$.

Combining Eqs. (A.2) and (A.4) and integrating, we get:

$$\ln e_s = \frac{c_{pv} - c_{pl}}{R_v} \ln T - \frac{C_1}{R_v}\frac{1}{T} + C_2, \tag{A.5}$$

with e_s in hPa. The integration constant C_2 can be obtained by evaluating Eq. (A.5) at T=273.15 K, where e_s is 6.11 hPa [3]. This gives C_2=55.2789. Rewriting Eq. (A.5), yields:

$$e_s = T^{\frac{c_{pv}-c_{pl}}{R_v}} \exp\left[-\frac{C_1}{R_v}\frac{1}{T} + C_2\right]. \tag{A.6}$$

After substituting the values for the different parameters, this becomes:

$$e_s = T^{-5.088} \exp\left[-\frac{6.809 * 10^3}{T} + 55.28\right]. \tag{A.7}$$

In order to come to an expression of the saturation specific humidity, we will first give the equation for the specific humidity:

$$q = \frac{\rho_v}{\rho_d + \rho_v}. \tag{A.8}$$

In the atmosphere, the density of water vapour (ρ_v) is much smaller than the density of dry air (ρ_d), so we approximate the specific humidity by:

$$q \approx \frac{\rho_v}{\rho_d}. \tag{A.9}$$

Using the ideal gas law, this can be written as:

$$q \approx \frac{p_v}{p_d}\frac{R_d}{R_v}, \tag{A.10}$$

in which R_d is the gas constant for dry air, 287.04 $\mathrm{Jkg^{-1}K^{-1}}$. If the atmosphere is saturated with respect to water vapour, the expression for the saturation humidity becomes:

$$q_s \approx \frac{e_s}{p_d}\frac{R_d}{R_v}. \tag{A.11}$$

Substituting Eq. (A.7) yields:

$$q_s(T) \approx \frac{R_d}{R_v}\frac{T^{-5.088}}{p_d} \exp\left[-\frac{6.809 * 10^3}{T} + 55.28\right]. \tag{A.12}$$

The temperature and the pressure (in hPa) at each HIRLAM output level are input to T and p_d in Eq. (A.12). Finally, multiplying q_s with the relative humidity gives the actual specific humidity.

Appendix B

Justification of the radiation path

In the simple radiative transfer model, the radiance at the top of the atmosphere is calculated for a vertical air column. So, the value belongs to the top of the atmosphere right above the gridpoint at the earth's surface. However, if we want to compare the synthetic water vapour images with real water vapour images from Meteosat (first generation), we should not deal with the radiation that travels vertically upward. We should deal with the radiation that travels upward from the earth's surface in a slantwise manner in the direction of the sensor of the Meteosat satellite, that is located 36000 km above the equator. Actually it is more complex, because the radiation is refracted a bit during its path through the atmosphere, but we will neglect this. For our purpose, we will show that we find it justified to calculate the radiation at the top of the atmosphere as if it traveled a path perpendicular to the surface.

In Fig. B.1, the position of Meteosat relative to the earth is schematically presented (the scale is not perfect), along with the calculated and actual path of upwelling radiation. Since the height of the satellite and the radius of the earth are known, H_{sat} is 36000 km and r_a is 6370 km, we are able to calculate the angle α for every latitude β. This is given by:

$$\alpha = 180° - \delta - \gamma. \tag{B.1}$$

Since S' is the perpendicular projection of S on MO, γ follows directly from:

$$\gamma = 180° - 90° - \beta.$$

In order to calculate δ, we need to know two sides of the right triangle MSS'. SS' can be easily deduced from the right triangle OSS', where SO is equal to r_a:

$$SS' = SO \sin \beta.$$

The same triangle gives us:

$$OS' = SO \cos \beta,$$

which we need in:

$$MS' = MO - OS',$$

in which MO is 42370 km ($H_{sat} + r_a$). Now that we know SS' and MS', δ can be derived from:

$$\tan \delta = \frac{MS'}{SS'}.$$

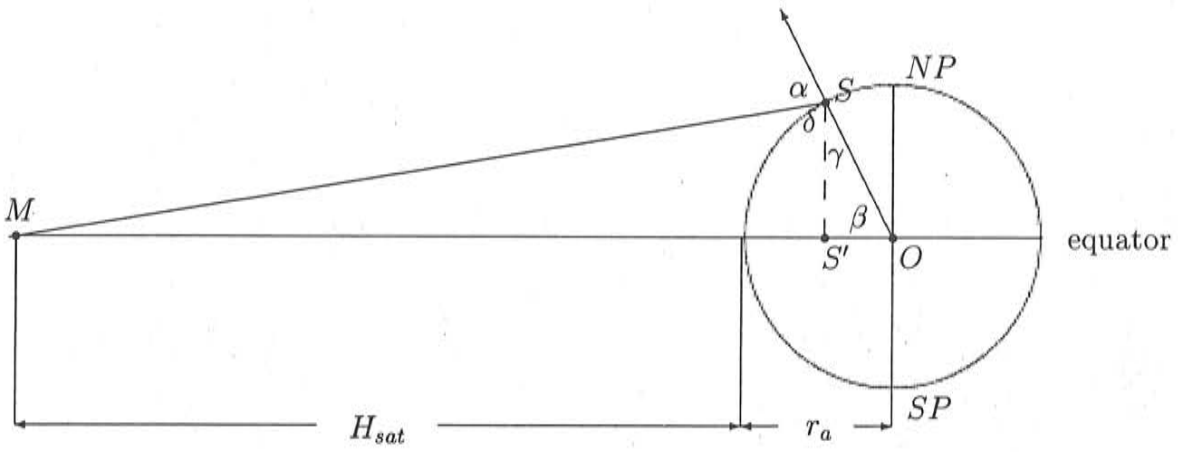

Figure B.1: *Schematic overview of the earth - Meteosat satellite system. Meteosat (M) is situated at a height H_{sat} above the equator of the earth. NP presents the north pole, SP the south pole and O is the centre of the earth. The radius of the earth is given by r_a. Point S is situated at the earth's surface with latitude β. S' is the perpendicular projection of S on the line MO. The arrow from O through S presents the upwelling radiation from the surface (S) as is calculated by the model. However, if we neglect the refraction in the atmosphere, the actual path of the radiation would go right from S to M. α is the angle between OS and SM, δ is the angle between SM and SS' and γ is the angle between OS and SS'.*

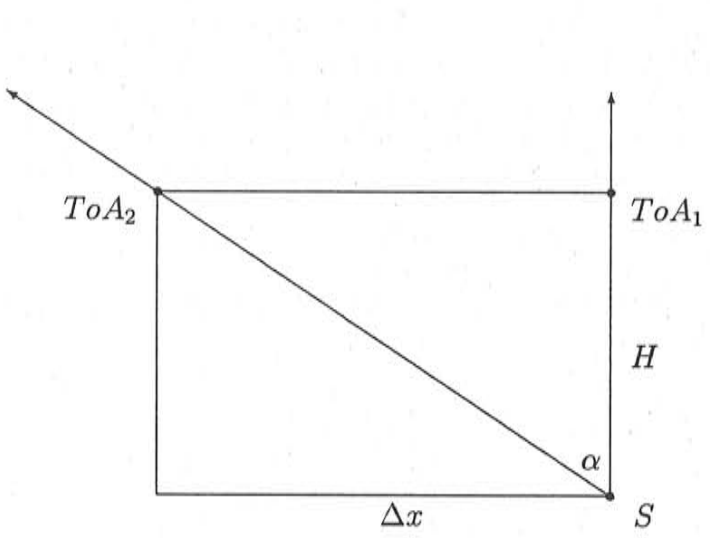

Figure B.2: *Rectangle that represents the atmosphere through which the radiation travels upwards from point S at the earth's surface perpendicularly to the top of the atmosphere ToA_1 (and further) and slantwise in the direction of the Meteosat satellite (M) up to ToA_2 (and further). H is the height of the atmosphere, in which absorption by water vapour occurs (from the surface to the top of the atmosphere) and Δx is the horizontal displacement if the slantwise path is considered. α is the angle between the perpendicular path and the slantwise path, just as in Fig. B.1.*

Substituting γ and δ into Eq. (B.1), we find that the angle between the calculated and actual path depends only on latitude β:

$$\alpha = 90° + \beta - \arctan\left(\frac{(H_{sat} + r_a) - r_a \cos\beta}{r_a \sin\beta}\right). \tag{B.2}$$

For example, if β is 50°, α will be 57.3°. If the latitude exceeds 80°, the satellite could not be reached by a direct path anymore.

In Fig. B.1, the atmosphere can not be distinguished, because the height of the atmosphere, H, is very small relative to the radius of the earth ($H \ll r_a$). Therefore, we may neglect the curvature of the earth and consider the atmosphere, in which the calculated and actual path of the upwelling radiation lie, as a rectangle. This is presented in Fig. B.2.

The horizontal displacement Δx is given by:

$$\Delta x = H \tan\alpha. \tag{B.3}$$

For the latitude range 0° to 80°, the horizontal displacement factor, $\tan\alpha$, is plotted in Fig. B.3. The horizontal displacement factor increases with latitude, which comes as no surprise.

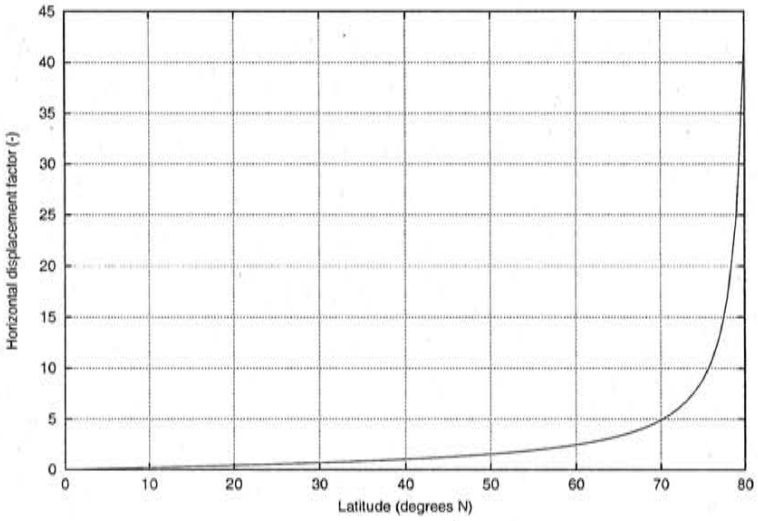

Figure B.3: *Horizontal displacement factor as a function of latitude β.*

At 39°, the factor is 1, so the displacement is equal to the H, the height of the atmosphere, in which absorption by water vapour occurs. At 60°, the factor has grown to 2.5, while at 70° it is 5. Approaching 80°, the factor becomes infinitely high. If we want to know the real displacement Δx, we need to know H. As we have seen in our experiments, in case of moist upper atmospheres, radiation can be absorbed up to some 200 hPa. In a standard atmosphere, the height of the 200 hPa surface is 11.8 km [5]. At high latitudes, H will be smaller than at low latitudes, because the height of the tropopause is lower. If we keep in mind that the horizontal resolution of the HIRLAM model we work with, is 55 km, we can deduce that only at latitudes above some 65°, Δx may exceed the model resolution. So, only for these latitudes we should perhaps work with the model values of the neighbouring

gridpoint(s) higher in the atmosphere. In our study, we show radiance or brightness fields up to 75°N. There, Δx is 9 times H, which means that we should use the values of only one neighbouring gridpoint. Besides, we will not focus on these high latitudes. Therefore, we find it justified to calculate the radiance at the top of the atmosphere in each gridpoint as if it travels upward perpendicular to the earth's surface.

Appendix C

Source code program "RT model"

```
      Program RT_model
C**   Radiative transfer model

C**   this program calculates the brightness temperature from the HIRLAM
c     pressure, temperature and humidity data for an air column, using radiative
c     transfer theory, assuming that clouds are absent. At 26 levels, with
c     equal pressure intervals in between, the spectral radiation, that will be
c     converted to a brightness temperature, is calculated.

ccccccccccccccccccccccccccccccccccccccccccccccccccccccccccccccccccccccccccc

C** DECLARATIONS

C** ARRAY DAT contains values for 3 variables for levels i=1,nlev.
c i=1 is upper level, i=nlev is surface level.
c variables:
c   1: Pressure (Pa)
c   2: Temperature (K)
c   3: Specific humidity (kg kg^-1)

      integer nlev
      parameter (nlev=26)
      real DAT(nlev,3)

C** FUNCTIONS
      real Abs_coef,Black,Brightness
      external Abs_coef,Black,Brightness

C** CONSTANTS specified by user
c   CC: Constant in absorption coefficient calculation (m^2 kg^-1)
c   nu: Wavenumber (m^-1)
```

```
      real CC,nu
      parameter (CC=14.0, nu=1590.0E2)

C** CONSTANTS
c   h:  Planck constant (kg m^2 s^-1)
c   c:  Velocity of light (m s^-1)
c   Kb: Boltzmann constant (kg m^2 K^-1 s^-2)
c   p0: Reference pressure (Pa)
c   T0: Reference temperature (K)
c   g:  Gravitational Acceleration (m s^-2)

      real h,c,Kb,p0,T0,g
      parameter (h=6.626176E-34,c=2.99792458E8,Kb=1.380662E-23,
     +           p0=1.0E5,T0=300.0,g=9.80616)


C** Variable that gives the location (= directory)

      character Loc*6

c** Variable that gives the number of points

      integer npoints

ccccccccccccccccccccccccccccccccccccccccccccccccccccccccccccccccccccccccc

C** MAIN PROGRAM

      call Init(DAT,nlev,npoints,Loc)

      call pro(DAT,nlev,npoints,CC,nu,bandwidth,h,c,Kb,p0,T0,g,Loc)

 222  end

ccccccccccccccccccccccccccccccccccccccccccccccccccccccccccccccccccccccccc

C** SUBROUTINE that reads in and determines all values of the array DAT

      Subroutine Init(DAT,nlev,npoints,Loc)

      integer nlev,npoints
      real DAT(nlev,3)
      character Loc*(*)
```

```
      real pres(nlev),temp(nlev)

      write (*,*) 'Give location'
      read (*,fmt='(A)') Loc

      if(Loc.eq.'gibral' .or. Loc.eq.'biscaj') then
         open(unit=1, file=Loc//'/11_2003031706')
         open(unit=2, file=Loc//'/51_2003031706')
      else
         open(unit=1, file=Loc//'/11_2003042300')
         open(unit=2, file=Loc//'/51_2003042300')
      end if

      write(*,*) 'Give number of points'
      read(*,*) npoints

C** reading pressure (hPa) from model
      read(unit=1,fmt=101) (pres(i),i=1,nlev)
  101 format (10X,F14.9,18X)
      rewind (unit=1)

C** converting pressure from hPa into Pa
      do i=1,nlev
         DAT(i,1)=pres(i)*100.0
      enddo

C** reading temperature (Celsius) from model
      read(unit=1,fmt=102) (temp(i),i=1,nlev)
  102 format (29X,F13.9)

C** converting temperature from Celsius into Kelvin
      do i=1,nlev
         DAT(i,2)=temp(i)+273.16
      enddo

C** reading specific humidity (q) (kg kg^-1) from model
      read(unit=2,fmt=102) (DAT(i,3),i=1,nlev)

 333  end

ccccccccccccccccccccccccccccccccccccccccccccccccccccccccccccccccccccccccccc

C** SUBROUTINE that determines the pressure of the 26 evaluation
c    levels and calculates the brightness temperature at these levels.
```

```
      Subroutine pro(DAT,nlev,npoints,CC,nu,bandwidth,h,c,Kb,p0,T0,g,
     +                                                          Loc)

      integer nlev,npoints
      real DAT(nlev,3)
      character Loc*(*)
      real CC,nu,bandwidth,h,c,Kb,p0,T0,g
      real ps,ptop,deltaP_prof,Ts,p_ev,T_ev,q_ev,rd,Tb
      external Brightness

C** output file with at each evaluation pressure level, values for the air
c temperature, the brightness temperature and the spectral radiance.
      open(unit=3,file=Loc//'/rtmodel')

      ps=DAT(nlev,1)
      ptop=DAT(1,1)
      deltaP_prof=(ps-ptop)/float(25)

      do i=1,26
         p_ev=ptop+deltaP_prof*(i-1)
         call TSH(nlev,DAT,p_ev,T_ev,q_ev)
         call rad(DAT,nlev,npoints,CC,nu,h,c,Kb,p0,T0,g,p_ev,rd,Loc)
         Tb=Brightness(h,c,Kb,nu,rd)
         write(unit=3,fmt=103) p_ev,T_Ev,Tb,rd
 103     format(F9.2,1X,F9.4,1X,F9.4,1X,F20.6)
      enddo

 444  end

ccccccccccccccccccccccccccccccccccccccccccccccccccccccccccccccccccccccccc

C** SUBROUTINE that determines the pressure of the 'npoints' discretization
c   levels and calculates the total spectral radiance at these levels.

      Subroutine rad(DAT,nlev,npoints,CC,nu,h,c,Kb,p0,T0,g,p_ev,rd,Loc)

      integer nlev,npoints
      real DAT(nlev,3)
      real CC,nu,h,c,Kb,p0,T0,g
      real p_ev,rd
      real p_up,p_low,T_up,T_low,q_up,q_low,k_up,k_low,B_up,B_low
      real ps,deltaP,Ts,Bs,opt_tot,earth_cont,atm_cont
      external Black,Abs_coef
```

```
      character Loc*(*)

      ps=DAT(nlev,1)
      Ts=DAT(nlev,2)
      deltaP=(ps-p_ev)/float(npoints-1)
      Bs=Black(nu,h,c,Kb,Ts)
      call opd(DAT,nlev,npoints,CC,p0,T0,g,p_ev,ps,opt_tot)
      earth_cont=Bs*exp(-1.*opt_tot)

C** output file with for each discretization interval, values for the mean
c   pressure, the mean optical depth and the contribution of the interval to the
c   total spectral radiance.
      open(unit=4,file=Loc//'/rtmodel_cont')

C** calculation of the atmospheric contribution, by summing over all interval
c   contributions.

      p_up=p_ev
      p_low=p_ev+deltaP
      call TSH(nlev,DAT,p_up,T_up,q_up)
      call TSH(nlev,DAT,p_low,T_low,q_low)
      B_up=Black(nu,h,c,Kb,T_up)
      B_low=Black(nu,h,c,Kb,T_low)
      k_up=Abs_coef(CC,p0,T0,p_up,T_up)
      k_low=Abs_coef(CC,p0,T0,p_low,T_low)
      call opd(DAT,nlev,npoints,CC,p0,T0,g,p_ev,p_up,opd_up)
      call opd(DAT,nlev,npoints,CC,p0,T0,g,p_ev,p_low,opd_low)
      atm_cont=(0.5/g)*(k_up*q_up*B_up*exp(-1.*opd_up)+
     +                  k_low*q_low*B_low*exp(-1.*opd_low))*deltaP
      write(4,*) (p_up+p_low)/2.,(opd_up+opd_low)/2.,atm_cont

      do j=2,npoints-1
         p_up=p_low
         T_up=T_low
         q_up=q_low
         p_low=p_ev+deltaP*(j)
         call TSH(nlev,DAT,p_low,T_low,q_low)
         B_up=B_low
         B_low=Black(nu,h,c,Kb,T_low)
         k_up=k_low
         k_low=Abs_coef(CC,p0,T0,p_low,T_low)
         call opd(DAT,nlev,npoints,CC,p0,T0,g,p_ev,p_up,opd_up)
         call opd(DAT,nlev,npoints,CC,p0,T0,g,p_ev,p_low,opd_low)
         atm_cont=atm_cont+(0.5/g)*(k_up*q_up*B_up*exp(-1.*opd_up)+
```

```
     +                 k_low*q_low*B_low*exp(-1.*opd_low))*deltaP
         write(4,*) (p_up+p_low)/2.,(opd_up+opd_low)/2.,
     +              (0.5/g)*(k_up*q_up*B_up*exp(-1.*opd_up)+
     +               k_low*q_low*B_low*exp(-1.*opd_low))*deltaP
      enddo

      write(4,*)

      rd=earth_cont+atm_cont

 555  end

ccccccccccccccccccccccccccccccccccccccccccccccccccccccccccccccccccccccccc

C** SUBROUTINE that determines the pressure of the 'npoints' optical depth
c   discretization levels and calculates the optical depth between the higher
c   height PH and the lower height PL

      Subroutine opd(DAT,nlev,npoints,CC,p0,T0,g,PH,PL,optd)

      integer nlev,npoints
      real DAT(nlev,3)
      real CC,nu,h,c,Kb,p0,T0,g
      real PH,PL,optd
      real dP,opd_part
      real p_up,p_low,T_up,T_low,q_up,q_low,k_up,k_low,B_up,B_low
      external Abs_coef

      dP=(PL-PH)/float(npoints-1)

      p_up=PH
      p_low=pH+dP
      call TSH(nlev,DAT,p_up,T_up,q_up)
      call TSH(nlev,DAT,p_low,T_low,q_low)
      k_up=Abs_coef(CC,p0,T0,p_up,T_up)
      k_low=Abs_coef(CC,p0,T0,p_low,T_low)
      opd_part=(0.5/g)*(k_up*q_up+k_low*q_low)*dP

      do k=2,npoints-1
         p_up=p_low
         T_up=T_low
         q_up=q_low
         p_low=PH+dP*(k)
         call TSH(nlev,DAT,p_low,T_low,q_low)
```

```
         k_up=k_low
         k_low=Abs_coef(CC,p0,T0,p_low,T_low)
         opd_part=opd_part+(0.5/g)*(k_up*q_up+k_low*q_low)*dP
       enddo

       optd=opd_part

 666   end

ccccccccccccccccccccccccccccccccccccccccccccccccccccccccccccccccccccccccccccc

       SUBROUTINE TSH(np,ee,xx,yy,zz)
c**    this routine calculates the temperature and
c**    specific humidity from the profile ee by linear
c**    interpolation between the given values
c**    version 20030905-1 wim verkley
       dimension ee(np,4)
       pt=ee( 1,1)
       ps=ee(np,1)
       if (xx.le.pt) goto 4
       if (xx.ge.ps) goto 5
       i=0
     3 i=i+1
       if (i.ge.np) stop
       x1=ee(i+0,1)
       x2=ee(i+1,1)
       y1=ee(i+0,2)
       y2=ee(i+1,2)
       z1=ee(i+0,3)
       z2=ee(i+1,3)
       if ((x1.le.xx).and.(xx.le.x2)) goto 2
       goto 3
     2 yy=y1+((xx-x1)/(x2-x1))*(y2-y1)
       zz=z1+((xx-x1)/(x2-x1))*(z2-z1)
       goto 6
     4 yy=ee(1,2)
       zz=ee(1,3)
       goto 6
     5 yy=ee(np,2)
       zz=ee(np,3)
     6 continue
       return
 777   end
```

```
ccccccccccccccccccccccccccccccccccccccccccccccccccccccccccccccccccccccccc
C** FUNCTION that calculates the brightness temperature from spectral radiance
      real Function Brightness (h,c,Kb,nu,radiance)
      real h,c,Kb,nu,radiance,ln_factor
      ln_factor=LOG(2.0*h*(c**2)*(nu**3)/radiance+1.0)
      Brightness=h*c*nu/(Kb*ln_factor)
      end
ccccccccccccccccccccccccccccccccccccccccccccccccccccccccccccccccccccccccc
C** FUNCTION that calculates the absorption coefficient
      real Function Abs_coef(CC,p0,T0,p,T)
      real CC,p0,T0,p,T
      Abs_coef=CC*((p/p0)**0.9834)*((T0/T)**-2.5294)
      end
ccccccccccccccccccccccccccccccccccccccccccccccccccccccccccccccccccccccccc
C** FUNCTION that calculates the black body radiation
      real Function Black (nu,h,c,Kb,T)
      real nu,h,c,Kb,T
      Black=(2.0*h*(c**2)*(nu**3))/(exp(h*c*nu/(Kb*T))-1.0)
      end
```

Appendix D

Source code program "Tijm adapted"

```
      Program Tijm_adapted

C**   this program calculates the brightness temperature from the HIRLAM
c     pressure, temperature and humidity data for an air column, using an
c     equation developed by Sander Tijm (KNMI) that has been adapted to include
c     the pressure and temperature dependence of the absorption. At the 26
c     HIRLAM pressure levels, the brightness temperature is calculated.

ccccccccccccccccccccccccccccccccccccccccccccccccccccccccccccccccccccccccccc

C** DECLARATIONS

C** Array DATA contains values for nvar variables for levels i=1, nlev.
c** i=1 is upper level, i=nlev is surface level.
c** nvar variables:
c   1: pressure (Pa)
c   2: temperature (K)
c   3: specific humidity (kg kg^-1)

      integer nlev, nvar
      parameter (nlev=26, nvar=3)
      real DATA(nlev,nvar)

C** Constants specified by user
c   q_wv: treshold value

      real q_wv
      parameter (q_wv=0.85)

C** CONSTANTS
c   p0: Reference pressure (Pa)
```

```
c    T0: Reference temperature (K)

      real p0,T0
      parameter (p0=1.0E5,T0=300.0)

C** Array BRIGHT contains values of the brightness temperature

      real BRIGHT(nlev)

C** Variable that gives the location (= directory)

      character Loc*6

ccccccccccccccccccccccccccccccccccccccccccccccccccccccccccccccccccccccccccc

C** MAIN PROGRAM

      call Get_Values_DATA(DATA,nlev,nvar,Loc)

      call Twv(DATA,nlev,nvar,q_wv,BRIGHT,p0,T0)

      call Output(DATA,nlev,nvar,BRIGHT,Loc)

      end

ccccccccccccccccccccccccccccccccccccccccccccccccccccccccccccccccccccccccccc

C** SUBROUTINE that reads in the values for array DATA

      Subroutine Get_Values_DATA(DATA,nlev,nvar,Loc)

      integer nlev, nvar
      real DATA(nlev,nvar)

      character Loc*(*)

      real pres(nlev), temp(nlev)

      write (*,*) 'Give location'
      read (*,fmt='(A)') Loc

      if(Loc .eq. 'gibral' .or. Loc .eq. 'biscaj') then
         open(unit=1, file=Loc//'/11_2003031706')
         open(unit=2, file=Loc//'/51_2003031706')
```

```
      else
         open(unit=1, file=Loc//'/11_2003042300')
         open(unit=2, file=Loc//'/51_2003042300')
      end if

C** reading pressure (hPa) from model
      read (unit=1, fmt=101) (pres(i),i=1,nlev)
  101 format (10X,F14.9,18X)
      rewind (unit=1)

C** transforming pressure from hPa into Pa
      do 5, i=1,nlev
         data(i,1)=pres(i)*100
    5 continue

C** reading temperature (Celsius) from model
      read (unit=1, fmt=102) (temp(i),i=1,nlev)
  102 format (29X,F13.9)

C** transforming temperature from Celsius into Kelvin
      do 10, i=1,nlev
         data(i,2)=temp(i)+273.16
   10 continue

C** reading specific humidity (q) (kg/kg) from model
      read (unit=2, fmt=102)(data(i,3),i=1,nlev)

      end

ccccccccccccccccccccccccccccccccccccccccccccccccccccccccccccccccccccccccccc

C** SUBROUTINE that calculates the WV brightness temperature

      subroutine Twv(DATA,nlev,nvar,q_wv,BRIGHT,p0,T0)

      integer nlev, nvar
      real DATA(nlev,nvar),BRIGHT(nlev),q_wv,p0,T0
      real deltaP,q,T,p,Value_inbetween

c** Brightness temperature at the surface (nlev) = surface temperature

      BRIGHT(nlev)=DATA(nlev,2)

      write (*,*) BRIGHT(nlev)
```

```
      do 40, i=nlev-1,1,-1

         deltaP=(DATA(i+1,1)-DATA(i,1))/2.
         q=DATA(i+1,3)
         T=DATA(i+1,2)
         p=DATA(i+1,1)
         Value_inbetween=BRIGHT(i+1)*(1.-min(1.,q*deltaP/
     +           (q_wv*((p/p0)**-0.9834)*((T0/T)**2.5294))))
     +       +T*(min(1.,q*deltaP/
               (q_wv*((p/p0)**-0.9834)*((T0/T)**2.5294))))
         q=DATA(i,3)
         T=DATA(i,2)
         p=DATA(i,1)
         BRIGHT(i)=Value_inbetween*(1.-min(1.,q*deltaP/
     +           (q_wv*((p/p0)**-0.9834)*((T0/T)**2.5294))))
     +       +T*(min(1.,q*deltaP/
     +           (q_wv*((p/p0)**-0.9834)*((T0/T)**2.5294))))
         write (*,*) BRIGHT(i)
   40 continue

      end

ccccccccccccccccccccccccccccccccccccccccccccccccccccccccccccccccccccccccccc

C** SUBROUTINE that writes values of array DATA and BRIGHT to output file

      subroutine Output(DATA,nlev,nvar,BRIGHT,Loc)

      integer nlev,nvar
      real DATA(nlev,nvar),BRIGHT(nlev)

      character Loc*(*)

      open(unit=3, file=Loc//'/tijm_adap')

      do 50, i=1,nlev

         write (unit=3,fmt=104) (DATA(i,j), j=1,nvar), BRIGHT(i)
  104    format (3X,F9.2,3X,F9.4,3X,E14.7,3X,F9.4)

   50 continue

      end
```

Eerder gepubliceerde titels in de reeks *Intern Rapport*:

2000-01 Inventarisatie nowcasting-technieken voor gevaarlijk weer : eindrapport / *G.T. Geertsema, A. Maas, H.R.A. Wessels, H. Benschop, B. Blaauboer en C.J. Kok*

2000-02 COST-76 : aims, achievements and future / *W.A. Monna*

2000-03 Verslag van een studiereis naar de National Weather Service van de USA, juni 2000 / *A.W. Donker*

2000-04 Definitiestudie vervanging IBDS : eindrapport / *Sylvia Barlag, Hans Roozekrans, Richard Rothe, Jan Bijma, Jan Jans en Frans Debie*

2000-05 Rapportage voorstudie herinrichting Cabauw / *Projectgroep Voorstudie Herinrichting Cabauw*

2001-01 Neerslagonderzoek / *Foeke Kuik*

2001-02 Estimation of the maximum velocity of convective wind gusts / *Iwan Holleman*

2001-03 Synoptisch Waarneemnet Nederland 2000 (SWaNet NL 2000) / *J.P. van der Meulen*

2001-04 Eindrapport AutoTrend "Automatische generatie TREND 'S" / *Albert Jacobs*

2002-01 Sensitivity of the MAECHAM4 model to imposed ozone distributions / *Anne Grete Straume, Elisa Manzini and Peter Siegmund*

2002-02 Kwaliteitscriteria AVW / *H.R.A. Wessels*

2002-03 SAFIR beeldproduct voor real-time gebruik / *Iwan Holleman*

2003-01 LITE4ADM : on the use of LITE data for the Atmospheric Dynamics Mission Aeolus / *G.J. Marseille, A. Stoffelen en A. van Lammeren*

2003-02 Mistdetectie met satellietbeelden / *Peter Baas*

2003-03 Gecombineerde weergave van AMDAR en METAR / *O. van der Velde, I. Holleman, J. van der Meulen en S. Barlag*

2003-04 Three events of strong deep moist convection in The Netherlands / *P. Groenemeijer*

2003-05 KNMI HFDS data format specification, v. 3.5 / *H. Roozekrans and I. Holleman*

2003-06 Neerslaganalyse uit radar- en stationswaarnemingen / *I. Holleman*

2003-07 Synthetic water vapour images from the HIRLAM model using a radiative transfer model / *M.H. Voogt*

Bibliotheek KNMI
Postbus 201
3730 AE De Bilt
tel. 030 - 2 206 369
bibliotheek@knmi.nl